

University of Innsbruck
Faculty of Mathematics, Computer Science and
Physics

Department of Experimental Physics

Master Thesis

submitted for the degree of

Master of Science

Narrow-Line Cooling of Erbium and Dysprosium

by

Nefeli Ioli Sonnberger, BSc
Matriculation Nr.: 01632839

Submission Date: 7. September 2023
Supervisors: Univ.-Prof. Dr. Francesca Ferlaino

Abstract

This master thesis focusses on the optical setup of narrow-line cooling of the element erbium and dysprosium in the Er-Dy experiment. The purpose of this project is to cool an atomic cloud by applying narrow-line cooling instead of broad-line cooling, allowing us to achieve even lower temperatures and hence new research. The first part of the thesis deals with a summary of the theoretical basics of narrow-line cooling and the basic properties of the elements Er and Dy. Further, we describe the optical setup needed for narrow-line cooling, which consists of two lasers (741 and 841 nm) and a Stable Laser Systems (SLS) cavity, which is a very crucial part of the project to stabilise the lasers onto the desired frequency to address the correct transitions for narrow-line cooling. The stabilisation of the lasers is thus achieved by the Pound-Drever-Hall (PDH) locking technique. We performed measurements of the PDH signal for both lasers as well as cavity ring-down to characterise the cavity. Moreover, we searched for the transition of erbium according to theoretical values and found a transition, which we characterised by determining the linewidth and the g -factor. With the right transition, we then cooled the atomic cloud and observed how the temperature changes in the x- and y-direction to see how efficient we are cooling, and we performed 2D scan measurements measuring the atom number N and the cloud size σ_x alteration along the x-axis while varying the attenuation between 5 and 20 dB. With these measurements we could also plot a value proportional to the phase space density (PSD) and saw that our atomic cloud was cooled down. However, it should be mentioned that at the time where the measurements were recorded, we did not have sufficient atoms in the trap to have nice results. In addition, although the optical setup has also been built and aligned for dysprosium, no cooling measurements have been performed and analysed.

Zusammenfassung

Diese Masterarbeit befasst sich mit dem optischen Aufbau für das schmalbandige Laserkühlen für die Elemente Erbium und Dysprosium in dem Hauptexperiment Er-Dy. Der Zweck dieses Projekts ist das Kühlen einer Atomwolke mittels schmalbandiger Laserkühlung statt der Anwendung von breiten Linien. Dies erlaubt uns noch niedrigere Temperaturen zu erreichen und somit auch neue Forschung. Der erste Teil der Arbeit fasst die theoretischen Grundlagen des Laserkühlens, sowie die Basiseigenschaften der Elemente Erbium und Dysprosium zusammen. Weiters, wie erläutern den nötigen optischen Aufbau fürs schmalbandige Laserkühlen, welcher aus zwei Lasern (741 und 841 nm) und einem optischen Resonator (Stable Laser Systems (SLS)). Dieser Resonator spielt eine wichtige Rolle für dieses Projekt, denn dadurch werden die Laser auf die richtige Frequenz stabilisiert, um die richtigen Übergänge fürs schmalbandige Laserkühlen zu adressieren. Das Verfahren, welches in diesem Projekt zur Stabilisierung von den Lasern dient, heißt Pound-Drever-Hall (PDH). Um den Resonator zu analysieren haben wir verschiedene Messungen durchgeführt. Wir haben uns das PDH-Signal von beiden Lasern angeschaut sowie eine Resonator-Abklingspektroskopie gemessen. Als nächstes haben wir den richtigen Übergang für Erbium mittels theoretischen Werten gesucht und den gefundenen Übergang analysiert, indem wir die Linienbreite und den g -Faktor bestimmt haben. Mit dem richtigen Übergang haben wir dann die Atomwolke gekühlt und dabei beobachtet, wie sich die Temperatur in x - und y -Richtung ändert. Darüber hinaus haben wir 2D scan Messungen durchgeführt, wo wir die Atomanzahl N und die Änderung der Größe der Atomwolke σ_x entlang der x -Achse beobachtet haben, während einer Änderung der Lichtabnahme zwischen 5 und 20 dB. Mit diesen Messungen konnten wir auch einen Plot erstellen, wo wir die y -Achse zu einem proportionalen Wert zur Phasenraumdichte umgerechnet haben, um eine bessere Vorstellung vom Kühlen zu bekommen. Allerdings ist es wichtig zu erwähnen, dass zum Zeitpunkt der Messungen, hatten wir nicht genügend Atome in der Falle, um gute Resultate zu erhalten. Wichtig zu erwähnen ist auch, dass zwar der optische Aufbau auch für Dysprosium gemacht und der Laser ausgerichtet ist, jedoch wurden keine Messungen vom Kühlen durchgeführt.

Contents

1	Introduction	4
2	Narrow-Line Cooling of Er and Dy	6
2.1	Basic properties of Er and Dy	6
2.2	Laser-Cooling Transitions in Erbium and Dysprosium	9
2.3	Theoretical basics of Narrow-line cooling	10
2.3.1	Optical Molasses	10
2.3.2	Doppler-Cooling Limit	14
3	Optical Setup for Narrow-Line Cooling	16
3.1	Er-Dy Experiment	16
3.2	Lasers: 741 nm and 841 nm	18
3.3	Experimental Setup	19
3.3.1	Laser Setup	19
3.3.2	Cooling Setup	21
4	Cavity Setup	24
4.1	Theoretical Basics of Cavity Physics	24
4.2	Stable Laser Systems (SLS) Cavity	27
4.3	Pound-Drever-Hall (PDH) locking technique	28
4.4	Cavity Characterisation	32
4.4.1	PDH Signal	32
4.4.2	Cavity Ring-Down	33
5	Transition characterisation	36
5.1	Linewidth measurement and broadening mechanisms	38
5.2	Landé g-factor measurement	44
6	Cooling characterisation	46
6.1	Temperature measurements	46
6.2	Cooling results	49
7	Conclusion and Outlook	54
	Appendix A	56

1 Introduction

Laser cooling and trapping of neutral atoms have been a thriving field of research for several decades, enabling numerous breakthroughs in fundamental physics [1–5]. Traditional laser cooling techniques, like Doppler cooling, make use of broad atomic transitions. However, as atomic physics experiments require even colder temperatures to realise novel quantum states of matter, traditional methods sometimes fall short. The solution to this is narrow-line cooling, which is a method that uses much narrower atomic transitions and can thus reach even cooler temperature limits [6–8].

In the last few years the interest and research on narrow-line cooling has gained considerable momentum. Although it is more complex to implement compared to broad-line cooling, since the cooling lasers have to be stabilised to higher precision, achieving temperatures in the microkelvin or even nanokelvin range is a great reward. At these temperatures, novel quantum states can be observed and analysed, offering a deeper understanding of the fundamental properties of matter. Many groups around the world are focussing on the application of narrow-line cooling to study quantum states such as Bose-Einstein condensates (BECs) [9–11], Fermi degenerate gases [12, 13] and strongly correlated quantum gases [14]. Furthermore, narrow-line cooling is very important for precision measurements to test fundamental theories of physics [15–17]. In general, the idea and the primary motivation behind narrow-line cooling is the achievement of lower temperatures in comparison to the temperatures reached by Doppler cooling methods. This amplifies the precision of atomic experiments because cold atom clouds provide longer coherence times and reduced Doppler broadening, meaning that the spectroscopic features are sharper. Moreover, at extremely low temperatures, interactions between the atoms can be controlled and adjusted using external fields, leading to a desire to study such interactions and quantum states.

Narrow-line cooling has been researched on different elements such as alkali elements, for example, for Li [8], Li and Sr [18], Ca [19], Sr [20] but also for lanthanides, for example, for Er [21, 22], Dy [7] and Yb [23]. The different elements offer various atomic transitions. For instance, strontium and ytterbium have narrow transitions in the visible and near-infrared ranges, which can be used for cooling. Lanthanides are also compelling candidates for narrow-line cooling. Specifically erbium and dysprosium offer rich internal structures and its strong magnetic interactions make them partic-

ularly interesting for studies of quantum magnetism and dipolar gases [7, 22]. Both erbium and dysprosium have narrow electronic transitions that can be exploited for laser cooling. Due to their magnetic moments, these two elements can form quantum gases with long-range and anisotropic dipolar interactions, allowing physicists to research novel quantum phenomena that are inaccessible with traditional alkali atoms.

In summary, narrow-line cooling has become an important step in an experiment in the realm of ultra-cold atomic physics. Raising the temperature limits could bring about more intricate physics, greater accuracy, and a more profound comprehension of the quantum world. The versatility of this technique in the use of various elements, including lanthanides, ensures its place at the forefront of contemporary atomic research.

This thesis focusses on the implementation of narrow-line cooling of an ultra-cold experiment using the elements erbium and dysprosium and is divided into three main parts. The first part reviews the basic properties of Er and Dy, as well as their laser-cooling transitions. Moreover, the chapter is dedicated to the theory of narrow-line cooling. The second main part deals with the optical setup, which is necessary to achieve narrow-line cooling. In this chapter, the main experiment (Er-Dy) is briefly explained followed by the additional experimental setup, which includes two lasers (741 nm and 841 nm), since we are working with two different species. Furthermore, the cavity plays an important role in the setup, because the lasers need to be stabilised onto a specific frequency in order to address the correct transitions for narrow-line cooling. A short chapter also focusses on the Pound-Drever-Hall (PDH) technique, which is the most suitable locking technique for this experiment. The third main part deals with the analysis of the results of this experiment. We start with the characterisation of the cavity, where the PDH signal for both lasers and cavity ring-down measurements have been performed and analysed. Furthermore, we present the analysis results of the erbium transition characterisation we have observed, for which we have determined the linewidth and the g -factor to compare to their theoretical values. Finally, we present a cooling characterisation by observing temperature measurements and the cooling results and show if the project was successful or not.

2 Narrow-Line Cooling of Er and Dy

Laser cooling based on narrow-line transitions is a useful technique to cool down atoms to low temperatures and high phase-space densities. Narrow transitions in the range of kilohertz have the feature of a low Doppler temperature, meaning that temperatures of the order of nanokelvin can be easily achieved even without evaporative cooling. In fact, narrow-line cooling has been applied to the 1S_0 to 3P_1 transitions for the elements Mg [24], Ca [6, 25] and Sr [15, 26, 27].

The lanthanides erbium and dysprosium have a very complex energy spectrum with various narrow optical transitions. Moreover, a feature of both elements is their large magnetic moment in their electronic ground state, allowing the access to the field of strongly dipolar quantum gases, which is the main focus of the research group in Innsbruck.

In the following, I will briefly review the basic atomic properties of erbium and dysprosium as well as their energy level diagrams. Further, theoretical basics of narrow-line cooling, namely the technique of optical molasses and the Doppler-cooling temperature, are explained.

2.1 Basic properties of Er and Dy

Erbium (Er) and dysprosium (Dy) are rare-earth metals and belong to the lanthanide group of the periodic table of elements. Both elements are high abundant and are therefore important for technological applications. For example erbium is often used to decrease hardness of metals when alloyed with metals especially with vanadium [28]. Further, it is also used in erbium-doped fiber amplifiers, since Er^{3+} , meaning the triple ionised Er has transitions in the telecom windows. Moreover, Er is also used in lasers, as well as in photographic filters for the absorbance of infrared light [28, 29]. Dysprosium, on the other hand, is mainly used in alloys for neodymium-based magnets [30, 31], due to its resistance to demagnetisation at high temperatures. This feature is important for magnets used in motors, generators, wind turbines, electrical vehicles as well as in our mobile phones. The examples above show how often we use these elements in our everyday life without even realising it.

Figure 1 shows the elements from the lanthanide family. Erbium has an atomic number of $Z = 68$ and an atomic mass of $m_{\text{Er}} = 167.26$ amu, with the atomic mass unit $1 \text{ amu} = 1.660\,539 \times 10^{-27} \text{ kg}$. Dysprosium has an atomic number of $Z = 66$ and an atomic mass of $m_{\text{Dy}} = 162.50$ amu. Both elements have several bosonic as

well as fermionic stable isotopes, which are listed in Table 1.

Lanthanum 57 La 138.91	Cerium 58 Ce 140.12	Praseodymium 59 Pr 140.91	Neodymium 60 Nd 144.24	Promethium 61 Pm 145	Samarium 62 Sm 150.36	Europium 63 Eu 151.96	Gadolinium 64 Gd 157.25	Terbium 65 Tb 158.93	Dysprosium 66 Dy 162.50	Holmium 67 Ho 164.93	Erbium 68 Er 167.26	Thulium 69 Tm 168.93	Ytterbium 70 Yb 173.05	Lutetium 71 Lu 174.97
---------------------------------	------------------------------	------------------------------------	---------------------------------	-------------------------------	--------------------------------	--------------------------------	----------------------------------	-------------------------------	----------------------------------	-------------------------------	------------------------------	-------------------------------	---------------------------------	--------------------------------

Figure 1: The lanthanide series can be found at the very bottom of the periodic table and consists of 15 elements. Highlighted are the elements dysprosium with an atomic number $Z = 66$ and an atomic mass of $m_{\text{Dy}} = 162.50$ amu and erbium with $Z = 68$ and $m_{\text{Er}} = 167.26$ amu.

Table 1: Relative abundances and type of quantum mechanical statistics for all stable isotopes of erbium [28] and dysprosium [30].

	Isotope	Abundance (%)	Statistics
Erbium	^{162}Er	0.139	boson
	^{164}Er	1.601	boson
	^{166}Er	33.503	boson
	^{167}Er	22.869	fermion
	^{168}Er	26.978	boson
	^{170}Er	14.91	boson
Dysprosium	^{156}Dy	0.056	boson
	^{158}Dy	0.095	boson
	^{160}Dy	2.329	boson
	^{161}Dy	18.889	fermion
	^{162}Dy	25.475	boson
	^{163}Dy	24.896	fermion
	^{164}Dy	28.26	boson

The ground state electronic configuration of Er and Dy features a xenon core and can be written as:

$$[1s^2 2s^2 2p^6 3s^2 3p^6 3d^{10} 4s^2 4p^6 4d^{10} 5s^2 5p^6]_{\text{Xe}} 4f^m 6s^2,$$

where m indicates how many electrons occupy the open $4f$ shell. For erbium $m = 12$ and for dysprosium $m = 10$. Further, erbium has a total spin $S = 1$, an angular momentum $L = 5$ and a total angular momentum $J = 6$, leading according to Russel-Saunders coupling scheme $^{2S+1}L_J$ to the ground state $^3\text{H}_6$. For dysprosium the numbers are $S = 2$, $L = 6$, $J = 8$ and therefore the ground state $^5\text{I}_8$.

Due to the large total angular momentum of erbium ($J = 6$) and dysprosium ($J = 8$) of their ground state configuration, these elements have a large magnetic dipole

moment of $7 \mu_B$ for erbium and $10 \mu_B$ for dysprosium, where μ_B is the Bohr magneton and is defined as $\mu_B = \frac{e\hbar}{2m_e}$, with e the elementary charge and m_e the electron mass. This large magnetic moment is an additional basic property for both elements and makes them important for strong dipole-dipole interactions, since alkali atoms such as Rb, Cs or K have for instance magnetic moments in the order of $1 \mu_B$ in their ground state, whereas Sr, Ca, Yb have $0 \mu_B$ for their bosonic isotopes.

The interaction between two neutral particles is governed by the van der Waals interaction. However, in cold dilute gases only s -wave scattering between two atoms occur. Hence, the real interatomic potential can be replaced by a pseudo-potential, which depends on a single parameter, namely the s -wave scattering length a_s . This pseudo-potential is short range and isotropic and is called *contact interaction* and can be expressed as follows:

$$U_c(r) = \frac{4\pi\hbar^2 a_s}{m} \delta(r). \quad (1)$$

Further, the dipole-dipole interaction of particles polarised along a defined quantisation axis, can be described as

$$U_{dd}(r) = \frac{C_{dd}}{4\pi} \frac{1 - 3\cos^2(\theta)}{r^3}, \quad (2)$$

which either can be attractive for $\theta = 0$, meaning that the dipoles point head to tail, or repulsive for $\theta = \pi/2$, which means side by side. Here C_{dd} denotes the coupling constant, which for atoms with a permanent magnetic dipole moment μ , is equal to $\mu_0 \mu^2$, with μ_0 being the permeability of vacuum. For atoms with an electric dipole moment d , C_{dd} equals d^2/ϵ_0 , with ϵ_0 being the permittivity of vacuum. In a polarised system the parameter θ describes the angle between the interparticle axis and the direction of the polarisation. The strength of the dipolar interaction can be quantified by the coupling constant C_{dd} and the mass m of the particle through the following relation:

$$a_{dd} \equiv \frac{C_{dd}m}{12\pi\hbar^2}. \quad (3)$$

Further, the physical properties of a system are determined as the ratio of the dipolar length a_{dd} to the s -wave scattering length a_s :

$$\varepsilon_{dd} \equiv \frac{a_{dd}}{a_s} = \frac{C_{dd}}{3g}, \quad (4)$$

where g denotes the contact interaction parameter and is defined as $g = \frac{4\pi\hbar^2 a_s}{m}$. Com-

paring the relative strength of the dipole-dipole interaction of the lanthanide ^{164}Dy with the value $a_{\text{dd}}^{164\text{Dy}} = 132.7 a_0$ with the alkali ^{87}Rb with $a_{\text{dd}}^{87\text{Rb}} = 0.68 a_0$, where a_0 denotes the Bohr radius, shows immediately that lanthanides are ideal candidates for investigation of phenomena arising from the long-range and anisotropic dipole-dipole interaction [32].

2.2 Laser-Cooling Transitions in Erbium and Dysprosium

Erbium and dysprosium share many similarities in their atomic properties such as their melting point and mass, but also their energy level diagrams are alike as shown in Fig. 2. Compared to the spectrum of an alkali, these two energy level diagrams are way more complex, however they open up many opportunities to manipulate the atoms, due to the numerous transitions. For example, broad lines are characterised by $\frac{\Gamma}{\omega_R} \gg 1$, where Γ is the natural linewidth and ω_R the single-photon recoil frequency shift, which is defined as $\omega_R = \frac{\hbar^2 \Delta k^2}{2m}$, with Δk being the wavevector difference between the cooling and the atomic transition [26]. The different lines which vary from broad (MHz), to narrow (kHz) to even a Hz transition (e.g. for Erbium $\lambda_{\text{Er}} = 1299 \text{ nm}$ with a linewidth of $0.9(1) \text{ Hz}$ [33]), are used for various applications. Transitions can be split in different categories and used for different purposes depending on their natural linewidth. In our experiment, the broad transition to the singlet $^1\text{P}_1$ -configuration with the wavelength $\lambda_{\text{Er}} = 400.910 \text{ nm}$ for erbium and $\lambda_{\text{Dy}} = 421.290 \text{ nm}$ for dysprosium is used for the transversal cooling of the atomic beam, the Zeeman slower and for imaging.

In contrast, narrow lines are defined by $\frac{\Gamma}{\omega_R} \leq 1$ [26]. An example for a narrow transition is the one that couples to the triplet $^3\text{P}_1$ -configuration, with the wavelength $\lambda_{\text{Er}} = 582.842 \text{ nm}$ and a natural linewidth of $\Gamma = 2\pi \cdot 170 \text{ kHz}$ for erbium and $\lambda_{\text{Dy}} = 626.082 \text{ nm}$ with $\Gamma = 2\pi \cdot 135 \text{ kHz}$ for dysprosium and are used for the magneto-optical trap (MOT). Comparing the natural linewidth of the MOT transition of these two lanthanides to the MOT transition of the alkali ^{133}Cs $\text{D}_2(6^2\text{S}_{1/2} \rightarrow 6^2\text{P}_{3/2})$ for $\lambda_{\text{Cs}} = 852.35 \text{ nm}$ with $\Gamma_{\text{Cs}} = 2\pi \cdot 5.23 \text{ MHz}$ [35] we can notice how much narrower the transitions of the lanthanides are. However, there are even narrower transitions for example the transition in erbium with the wavelength $\lambda_{\text{Er}} = 841.22 \text{ nm}$ and in dysprosium with $\lambda_{\text{Dy}} = 740.96 \text{ nm}$ with the natural linewidths $\Gamma_{\text{Er}} = 2\pi \cdot 8.0 \text{ kHz}$ and $\Gamma_{\text{Dy}} = 2\pi \cdot 1.78 \text{ kHz}$. These two transitions are relevant for this thesis, since they are used for the narrow-line cooling. For comparison,

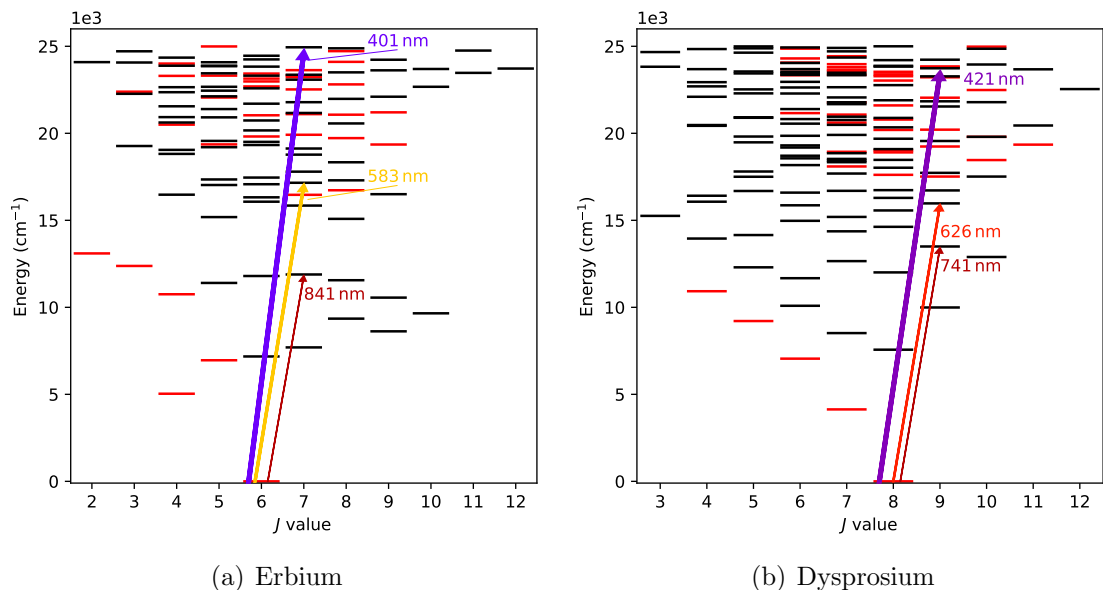


Figure 2: Energy spectrum of erbium (a) and dysprosium (b) [34] plotted as the energy depending on the total angular momentum J . The parity of the states is either even (red) or odd (black). The highlighted transitions represent the relevant transitions for this thesis. The transitions 401 nm, 421 nm are used for Zeeman slower (ZS), transversal cooling (TC) and imaging. The transitions 583 nm, 626 nm are implemented in the magneto optical trap (MOT) setup and the 841 nm and 741 nm transitions are suited for narrow-line cooling.

Table 2 shows the broadest along with the narrowest mentioned transitions of Er and Dy. In addition, the Doppler temperature $T_D = \frac{\hbar\Gamma}{2k_B}$, which limits the Doppler cooling, and the recoil temperature $T_r = \frac{\hbar^2 k^2}{2mk_B}$, which limits the sub-Doppler cooling, with k_B the Boltzmann's constant and $k = \frac{2\pi}{\lambda}$ wave vector, are listed for each transition. Fig.2 shows the energy level diagram of erbium (a) and dysprosium (b) as a function of the total angular momentum J . The parity, which describes the mirror symmetry of the states can be distinguished by the colour, where red stands for the even and black for the odd parity. The selection rules show that optical dipole transitions for example in erbium and dysprosium can only couple the ground state $J = 6$ to $J = [5, 7]$ and the state $J = 8$ to $J = [7, 9]$ [36]. The highlighted transitions are the relevant ones for the experiment.

2.3 Theoretical basics of Narrow-line cooling

2.3.1 Optical Molasses

It is known that if light shines on a substance, radiation pressure gets applied on this substance either via light reflection or light scattering. Hence, shining intense,

Table 2: Comparison of the Doppler and recoil temperatures of broad and narrow transitions for erbium and dysprosium [34, 37]. Interestingly, the Doppler temperature reaches different orders of magnitude for broad and narrow line cooling.

	Broad line cooling			Narrow line cooling		
Atom	Transition	$T_D[\mu\text{K}]$	T_r [nK]	Transition	$T_D[\text{nK}]$	$T_r[\text{nK}]$
^{168}Er	$6s^2\ ^3\text{H}_6 \rightarrow 6s6p^1\text{P}_1$ $\lambda = 400.91\ \text{nm}$ $\Gamma = 2\pi \cdot 29.4\ \text{MHz}$	707	350	$6s^2\ ^3\text{H}_6 \rightarrow ^4\text{I}_{15/2}^o 5d_{5/2} 6s^2$ $\lambda = 841.22\ \text{nm}$ $\Gamma = 2\pi \cdot 8.0\ \text{kHz}$	190	80.5
^{164}Dy	$6s^2\ ^5\text{I}_8 \rightarrow 6s6p^1\text{P}_1$ $\lambda = 421.290\ \text{nm}$ $\Gamma = 2\pi \cdot 32.2\ \text{MHz}$	774	329	$6s^2\ ^5\text{I}_8 \rightarrow ^6\text{H}^o 5d 6s^2\ ^5\text{K}_9$ $\lambda = 740.96\ \text{nm}$ $\Gamma = 2\pi \cdot 1.78\ \text{kHz}$	42.7	213

quasi-monochromatic laser light at a frequency near an atomic resonance on a low density gas can lead to cooling. This can be achieved due to the momentum which gets transferred from the atoms to the scattered light [38]. The idea of laser cooling was first studied in 1975 by two groups, Hänsch and Schawlow at Stanford University and Wineland and Dehmelt at the University of Washington. However, both groups used a slightly different method to slow down the movement of the atoms [39]. The Wineland-Dehmelt group succeeded laser cooling with the aid of the Raman process, where the Raman transitions can be used to remove kinetic energy from the atoms leading to cooling [39]. On the other hand, the Hänsch-Schawlow group managed to slow down the atoms using the Doppler effect, which describes the radiation pressure on an atom depending on its velocity. Therefore, they used six laser beams shining on a gas of atoms along each of the six Cartesian coordinate directions. The frequency of the lasers were tuned below the atomic resonance, leading the atoms to absorb light from the laser beams due to the Doppler shift and since the light comes from the opposite direction, it reduces the atoms movement, meaning that the temperature of the gas is reducing. Interestingly, due to the fact that red-tuned laser beams shine onto the gas of atoms from all directions, one can obtain a strong damping of the velocity similar to Brownian motion. Because of this effect on the atomic motion this method of laser cooling with the aid of the six-beam geometry, as shown in Fig. 3(a), is also known as optical molasses.

Nowadays, laser cooling is a very essential process in the research of the quantum physics range in order to bring atoms to their ground state and be able to examine different quantum phenomena, such as the creation of a Bose-Einstein condensate (BEC), which can be achieved by means of laser cooling followed by evaporative cooling.

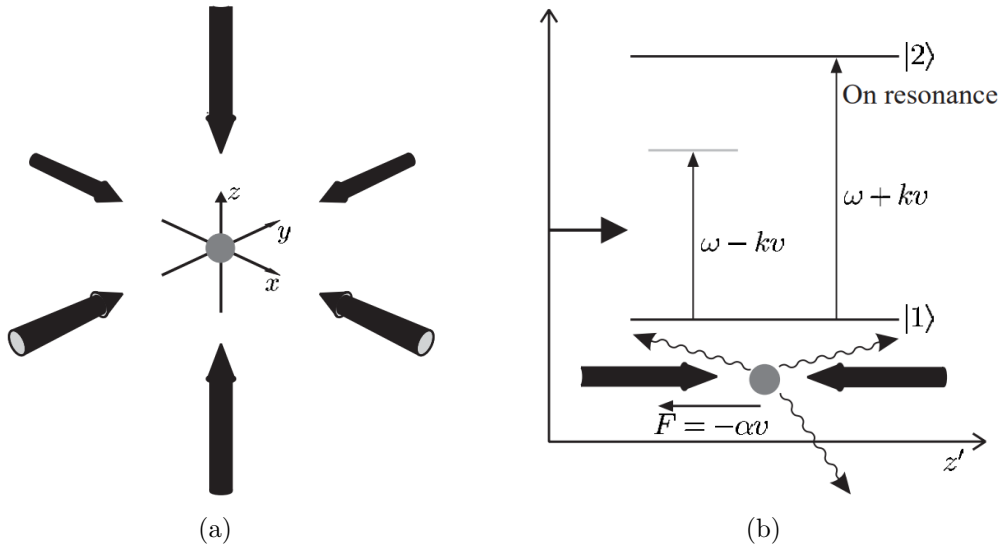


Figure 3: (a) The geometry of three pairs of counter-propagating laser beams, also known as optical molasses. (b) Rest frame of a moving atom with velocity v in one-dimensional optical molasses. The light gets scattered in the opposite direction of the atom's velocity due to the Doppler effect [36].

In this project, we are going to focus on a similar technique for laser cooling like the one of the Hänsch-Schawlow group. Here we are considering a one-dimensional optical molasses for simplicity, which cools down an axial motional degree of freedom of an atomic cloud to the Doppler limit by means of polarised light. It should be mentioned that optical molasses do not trap neutral atoms since there is no restoring force, different to an e.g. magneto-optical trap, which features a combination of light and magnetic field to keep them in place.

Lets now discuss the one-dimensional optical Molasses in more detail: Consider a two-level atom with a frequency ω_0 equal to the atomic transition between ground and excited state. This atom is located between a pair of counter-propagating beams, which are assumed to be plane waves with the wavelengths λ and an angular frequency ω . The detuning of the laser frequency can get determined by $\Delta = \omega - \omega_0$. In addition, these laser beams are tuned to a slightly lower frequency than the natural frequency of the atomic transition. If the atom is in motion with a velocity v as shown in Fig. 3(b), then the atom sees the laser frequency Doppler shifted by $kv = \frac{2\pi v}{\lambda}$, leading to a total detuning of $\Delta - kv$. Due to this Doppler effect, the atom moving towards the light source sees the light as blue-shifted meaning closer to its resonant frequency. The atom absorbs then photons from the light source and gains its momentum, which is in the opposite direction to the atom's momentum, meaning that the atom is slowed down. Then the atom spontaneously emits the photon in a

random direction. The momentum of this emission over a large number of atoms in an atomic cloud averages to zero. Further, Γ denotes the decay rate of the excited-state population to the ground state and the saturation intensity I_0 represents the laser-induced coupling between the excited and the ground state. These two factors are related to the Rabi frequency Ω as $\frac{I}{I_0} = \frac{2\Omega^2}{\Gamma^2}$. Additionally, the relation $\frac{h}{\lambda} = \hbar k$ describes the momentum per photon for light with a wavelength λ . Knowing these parameters the average force on an atom moving in the positive/negative direction is described by the average rate of absorbing photons times the momentum per photon, namely:

$$F_{\pm} = \pm \frac{\hbar k \Gamma}{2} \cdot \frac{s_0}{1 + s_0 + [2(\Delta \mp kv)/\Gamma]^2}, \quad (5)$$

where $s_0 = \frac{I}{I_0}$ is the saturation factor. This force is also known as radiation-pressure force or scattering force. By plotting the force F_{\pm} as function of the atom's velocity v , one gets a curve of the form as shown in Fig. 4. The blue curve represents F_+ , the red F_- and the black curve their sum.

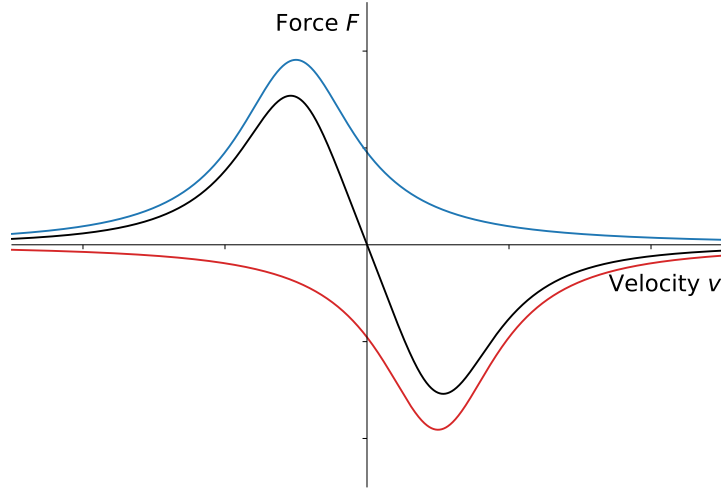


Figure 4: Force F as a function of the atom's velocity v . The blue and red curves represent the force carried by the counter-propagating beam on the atoms, according to Eq. (5), for F_- and F_+ , respectively. The black curve is the net force.

Furthermore, the force on atoms in optical molasses can be determined by $F_{\text{molasses}} = F_+ + F_-$ by assuming that the two counter-propagating beams are affecting the atoms independently. However, this assumption holds for a two-level system only if we are at a low intensity range meaning $s_0 = I/I_0 \ll 1$ leading to the following equation:

$$F_{\text{molasses}} = \frac{\hbar k \Gamma}{2} \frac{s_0 k v}{\Gamma} \cdot \frac{16\Delta/\Gamma}{1 + \frac{8}{\Gamma^2}(\Delta^2 + k^2 v^2) + \frac{16}{\Gamma^4}(\Delta^2 - k^2 v^2)^2}. \quad (6)$$

Further, assuming low velocities, we can use the approximation $|kv| \ll \Gamma, |\Delta|$, yielding:

$$F_{\text{molasses}} = 4\hbar k^2 v s_0 \frac{(2\Delta/\Gamma)}{(1 + (2\Delta/\Gamma)^2)^2} \equiv -\alpha v, \quad (7)$$

From the damping force $F_{\text{molasses}} = -\alpha v$ the damping coefficient α can be calculated as:

$$\alpha = -4\hbar k^2 s_0 \frac{(2\Delta/\Gamma)}{[1 + (2\Delta/\Gamma)^2]^2}, \quad (8)$$

with a maximum damping at $2\Delta/\Gamma = -1/\sqrt{3}$ [36, 39].

2.3.2 Doppler-Cooling Limit

Regarding the damping force $F_{\text{molasses}} = -\alpha v$, a rate of losing kinetic energy can be calculated by:

$$(dE/dt)_{\text{cool}} = Fv = -\alpha v^2. \quad (9)$$

Furthermore, the cooling rate is proportional to the kinetic energy, which leads to an energy-loss time constant and a velocity-damping time constant:

$$\tau_{\text{cool}} = -\frac{E}{(dE/dt)_{\text{cool}}} = \frac{m}{2\alpha}, \quad \tau_{\text{damp}} = -\frac{v}{(dv/dt)_{\text{cool}}} = \frac{m}{\alpha}. \quad (10)$$

In case of heating caused by the laser, for example due to absorption and emission of photons and by using the approximation $|kv| \ll |\Delta|, \Gamma$ and $I/I_0 \ll 1$ we can determine the heating rate:

$$(dE/dt)_{\text{heat}} = \frac{\hbar^2 k^2}{m} \Gamma \frac{I/I_0}{1 + (2\Delta/\Gamma)^2}, \quad (11)$$

showing that the heating rate depends only on the intensity and the detuning, while the cooling rate depends on the velocity. A balance between the heating and the cooling rate would lead to an equilibrium of the form $(dE/dt)_{\text{heat}} + (dE/dt)_{\text{cool}} = 0$. Transforming this equation to v^2 , which gives us either the mean square velocity of a gas of atoms during laser cooling or the time average of the squared velocity of a single atom, we get the form:

$$v^2 = \frac{\hbar\Gamma}{4m} \frac{1 + (2\Delta/\Gamma)^2}{2|\Delta|/\Gamma}. \quad (12)$$

Writing the kinetic energy term as $E_{kin} = \frac{1}{2}k_B T$ per degree of freedom, one can equate $\frac{1}{2}k_B T = \frac{1}{2}mv^2$, which in one dimension leads to:

$$k_B T = \frac{\hbar\Gamma}{4} \frac{1 + (2\Delta/\Gamma)^2}{2|\Delta|/\Gamma}. \quad (13)$$

According to Eq. (13) the temperature has a minimum when $2\Delta/\Gamma = -1$, then the so called Doppler temperature can be calculated as following

$$T_D = \frac{\hbar\Gamma}{2k_B}, \quad (14)$$

which is also known as the Doppler-cooling limit.

3 Optical Setup for Narrow-Line Cooling

This chapter focusses on the experimental setup for the narrow-line cooling of the mixture of Er and Dy and how the setup is connected to the main experiment. Since we are not focussing on one element, the setup is more challenging. However, we have the advantage that the transitions of Er and Dy with which we are working have a wavelength difference of 100 nm. This allows us to use optical elements, which are suitable for both wavelengths.

The chapter is divided into three sections and contains all the information about the setup. The first section gives a brief summary of how the main experiment works. The second section describes the main characteristics of the two lasers used in this project and lastly the experimental setup of the project is explained in the last section. Since in the lab we have an optical table with all the lasers and one optical table with the main apparatus, the setup is split on two tables as well. Hence, the last section is split into two subsections.

3.1 Er-Dy Experiment

The Er-Dy experiment focusses on experimental research of quantum gases of erbium and dysprosium or even a mixture of both elements. Fig. 5 shows the experimental apparatus, which was built over the years by several people.

The experiment starts with an oven, which is filled with a few grammes of solid pieces of Er and Dy. These are heated at a temperature of about 1100 °C and 1200 °C and are evaporated in an effusion cell, creating an atom vapour. The evaporated atoms are formed into an atomic beam with the aid of a series of apertures. The atomic beam is further collimated by 2D optical molasses, also called transverse cooling, using the laser light at 401 nm for erbium and 421 nm for dysprosium. After passing through the first gate valve, the atoms get through the atomic-beam-shutter section, which can be used in the experimental sequence to interrupt the atomic flux. In addition, the high-vacuum oven region is separated from the ultra-high-vacuum main chamber with the aid of a differential pumping section, which includes an ion pump, providing pressure in the region of 10^{-11} mbar.

After passing through the second gate valve, the atoms, which have an initial velocity of up to a few $100 \frac{m}{s}$, get slowed by a 350 mm long spin-flip Zeeman, slower to the required capture velocity of the MOT, which is around $5 \frac{m}{s}$. Here, we study the behaviour of dipolar atoms while a magnetic field B is applied. The atoms are then captured in a MOT using the 583 nm light for erbium and the 626 nm light

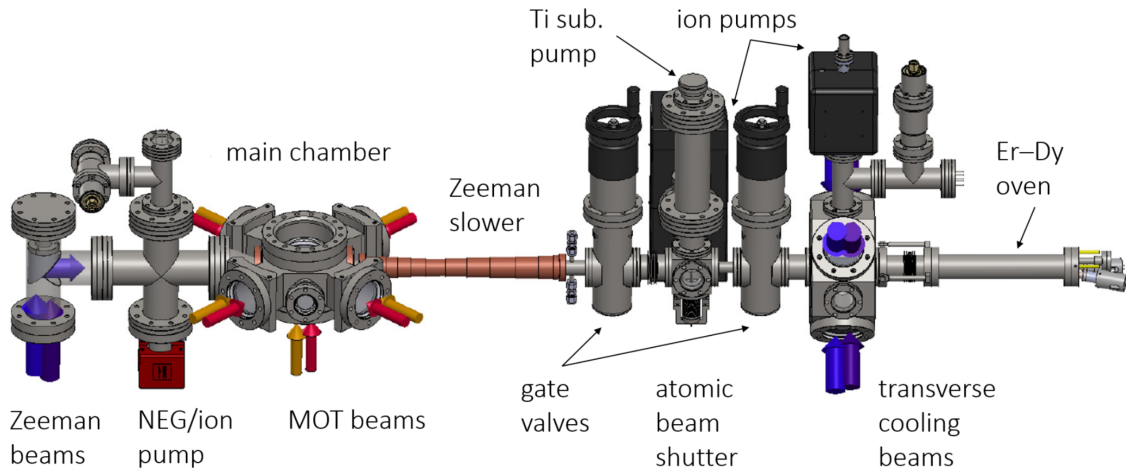


Figure 5: A sketch of the Er-Dy experimental apparatus. Solid pieces of Er and Dy get evaporated in the oven on the right, creating an atomic flux. Moreover the atomic beam travels to the left and gets collimated by transversal cooling (401 nm light for Er and 421 nm light for Dy). The atoms get slowed down in the Zeeman slower and enter the main chamber, where they get captured in the two-colour MOT (583 nm for Er and 626 nm for Dy). Figure taken from Ref. [40].

for dysprosium. This MOT consists of five beams instead of a standard MOT, which consists of six beams. The reason why one beam can be removed is the combination of narrow-line cooling and gravity [41, 42]. The atoms get gathered in the lower part of the MOT, where they are hit by light from the bottom and therefore automatically get spin-polarised in the lowest Zeeman sublevel, namely $m_J = -6$ for erbium and $m_J = -8$ for dysprosium. In addition, this five-beam configuration is very advantageous because it gives optical access from the top side of the chamber. Thus, high-resolution imaging optics are placed above the chamber [40]. After a typical MOT loading time of around 5 s, the cloud of approximately 5×10^7 atoms gets compressed by ramping the MOT parameters such as the power, magnetic field gradient, and detuning. After compression we reach temperatures as low as $\sim 10 \mu\text{K}$ for both atomic species [22, 41, 43].

The next step is to transfer the atoms into the ODT for evaporative cooling to quantum degeneracy. The ODT setup consists of three near-infrared (1064 nm) horizontal laser beams. Two beams (static ODT) have an approximately $60 \mu\text{m}$ waist and cross at a 90° angle. The third beam (scanning ODT) has a waist of $18 \mu\text{m}$ and can be rapidly scanned horizontally to create a variably anisotropic time-averaged potential [44]. When the atoms are loaded into the ODT, the MOT light is switched off, and a homogeneous magnetic bias field along the vertical axis is

adjusted to control the atomic scattering lengths. This is crucial because high two-body collision rates are needed for efficient evaporative cooling, while at the same time three-body collision rates should be low to avoid high losses. Moreover, the magnetic bias field is crucial for maintaining the spin polarisation of the atoms in the trap.

The experiment contains one further chamber, which is attached next to the main chamber and consists of a glass cell. This project is planned to be a quantum gas microscope for high-resolution imaging of Er and Dy. More details about the glass cell can be found in the doctoral thesis of Maximilian Sohmen [40].

More detailed information on the laser setups and the magnetic field coils of the Er-Dy experiment can be found in the doctoral thesis of Philipp Ilzhöfer [43]. Further, details on the magnetic field system can be read in the doctoral thesis of Gianmaria Durastante [45]. Moreover, information about the optical dipole trap (ODT) can be found in the Mastertheses of Simon Baier [46] and Claudia Politi [47].

3.2 Lasers: 741 nm and 841 nm

Since the experiment focusses on both atomic species erbium and dysprosium, two lasers with different wavelength ranges are necessary to work with the narrow transitions we are aiming for. Both lasers consist of a tunable diode laser with an integrated isolator with an extinction of around 63 dB from the company TOPTICA Photonics AG. The laser we are using to address the 841 nm transition can be tuned between 805 – 850 nm. The company's tests show that at a minimum wavelength of 804.59 nm the maximum power is 60.7 mW, at a gainmaximum of 838.83 nm the maximum power is 105.0 mW and at the maximum wavelength of 861.57 nm they measured a maximum power of 68.0 mW. In the lab, we measured for a wavelength around 841 nm a power of 36.5 mW. Accordingly, the laser used for the 741 nm transition can be tuned between 710 – 741 nm and the tests of the coarse tuning show that at a minimum wavelength of 709.93 nm a maximum power of 23.0 mW, at a gainmaximum of 727.31 nm a maximum power of 42.6 mW and at a maximum wavelength of 742.96 nm they tested to have 23.7 mW. In our case for a wavelength around 741 nm we measure with the power metre a power of 25.7 mW.

3.3 Experimental Setup

The main parts of this project are the two lasers and a cavity, which is crucial to lock the lasers to the needed frequency for the narrow transitions. The optical setup of the project consists of two parts. One part is an optical setup for the locking and is located on the optical table with the lasers. This setup is connected with an optical fibre to an additional smaller setup, which is near the apparatus and is necessary for the cooling of the atoms in the chamber. More information about the cavity and the locking technique that we are using in this project can be found in the next chapter.

3.3.1 Laser Setup

The lasers and the cavity are placed on a 60×90 cm breadboard, and since the paths of the lasers are similar, the setup is built symmetrical as shown in Fig. 6, where the schematic setup with all the needed optical elements is shown. We are

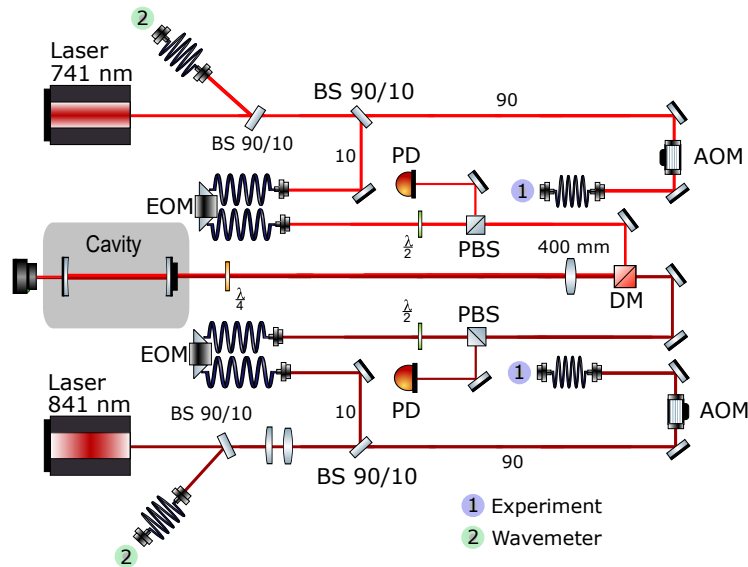


Figure 6: Schematic setup of the laser cooling system for Er and Dy. The setup is built symmetrically, and its three main parts are the two lasers and the cavity. The lower half of the setup shows the path of the 841 nm laser, which splits into three paths. One path leads to the wavemeter to check the frequency, the second path passes through an AOM to control the frequency of the light and the third path leads to a cavity in order to stabilise the laser frequency. The same setup can be found on the upper side for the 741 nm laser where it meets the 841 nm laser at a dichroic mirror.

going to focus on the path of the 841 nm laser in the bottom half of the picture,

since the 741 nm laser path is built in a similar way. The laser beam starts from the laser head and gets split by a 90/10 beamsplitter¹. The 10 % path passes through an optical fibre, which leads to a wavemeter (here indicated with the number two) to check the wavelength of the laser for the current and the piezo settings. The 90 % path passes through two cylindrical lenses, which shape the beam from an oval to a circular form. The laser beam is split again by a 90/10 beamsplitter, where the 90 % beam passes through an acousto-optic modulator² (AOM) to control the frequency of light. The light is then guided to the additional setup near the apparatus with the aid of an optical fibre (here indicated as number one). The 10 % path passes through a fibre-coupled integrated electro-optical modulator³ (EOM) to control the phase of the light. This path is crucial for the locking technique, which is explained in more detail in Chap. 4.3. Further, the light gets again split with the aid of a polarising beamsplitter (PBS) into a path, which gets to the cavity and the polarised from the cavity reflected light gets detected onto a photodiode⁴ (PD). In addition, a half-wave plate is positioned in front of each PBS to shift the polarisation, and a quarter-wave plate is placed in front of the cavity to get the right polarisation of the light reflected from the cavity. Lastly, a 400 mm lens is placed in front of the cavity to achieve a focal point at the centre of the cavity.

The beam of the 741 nm follows a very similar path as that of 841 nm with the only difference that the optical elements are chosen for the correct wavelength and hence the setup is symmetrical, as shown in the upper half of Fig. 6. Both beams meet at a long-pass dichroic mirror⁵ (DM), which has different reflexion/transmission properties at two different wavelengths and hence enables both laser beams to be guided to the cavity and back to the photodiodes. For instance, in our case the dichroic mirror is according to the Thorlabs data sheet for the wavelength 741 nm 97.72 % transmission and 2.07 % reflectance. For $\lambda = 841$ nm the transmission is 88.15 % and the reflectance 11.60 %. In order for this optical setup to work, we need several electronic devices such as radio-frequency (RF) amplifiers, direct digital synthesiser (DDS), EOM drivers and combiners. The setup of these parts is explained in the next chapter. Fig. 7 shows a photo of the laser setup with the path of the beams. Here, the most important optical elements and components such as the AOMs, EOMs, PDs, PBS's and BS are labelled with boxes so that one can

¹Thorlabs, BSF10-B, ARC 650 – 1050 nm

²Gooch & Housego PLC, 3080-125, centre frequency 80 MHz, bandwidth 25 MHz

³Jenoptik, PM785 for 741 nm laser, PM830 for 841 nm

⁴Thorlabs, PDA8A2, 320 – 1000 nm, 50 MHz BW

⁵Thorlabs, DMLP805, 805 nm Cut-On

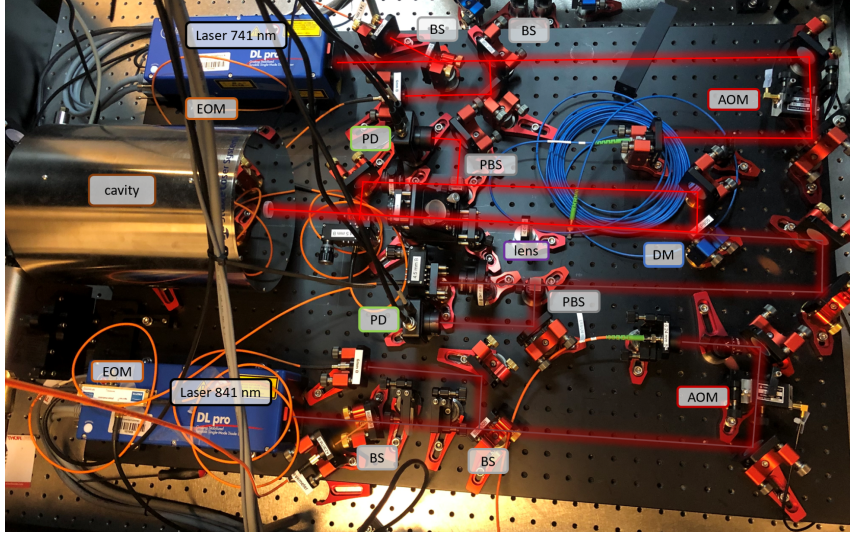


Figure 7: Photo of the setup of the laser cooling system for Er and Dy. The boxes indicate the most important optical elements and components to be able to compare with the schematic setup in Fig. 6. At the moment where the photo was taken, only the 841 nm laser was led to the cooling setup. Therefore, the blue optical fibre seen for 741 nm in the top right area of the picture is not connected to any fibre coupler.

compare with Fig. 6. In addition, since the opening of the cavity is at a height of around 125 mm, a periscope consisting of two mirrors was built to elevate the beam. Therefore, the last quarter-wave plate needed before the light enters the cavity is mounted on the periscope.

3.3.2 Cooling Setup

In order to bring the cooling laser light to the atoms an additional setup is necessary. In the previous paragraph, it is mentioned that a path of the laser light passes through an AOM and gets guided with the aid of an optical fibre to the setup next to the chamber. This setup consists of two fibre couplers, a PBS, a half-wave plate, and a few mirrors. One fibre coupler is used for both lasers 841/741 nm and the other for light coming from a 401 nm laser. The 401 nm transition is a strong transition and is used in this case as a tool to be able to align the beam of the 841/741 nm lasers. By aligning the resonant blue light on the atoms and making sure that the atoms are blown away as fast as possible, we have a reference beam hitting the atoms, which can be used to roughly align the narrow-line laser beams by overlapping them on the blue light. After checking that the atoms can be addressed with the narrow-line light, we added a mirror on the opposite side of the chamber as shown in Fig. 8, which creates a retro-reflected beam. This beam is then aligned

to create 1D Molasses in order to cool down an atomic cloud.

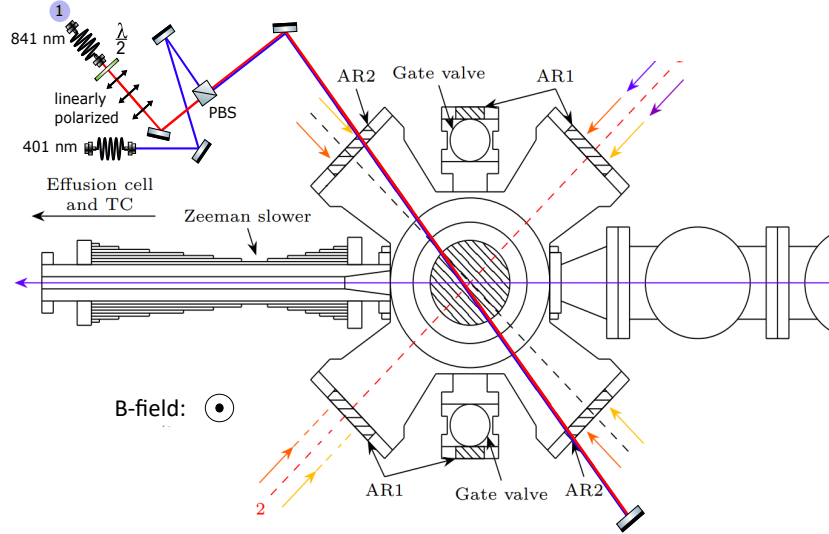


Figure 8: Schematic setup of the optical setup next to the chamber at the experimental table. The setup consists of a fibre coupler, a PBS and a few mirrors. The following setup without the mirror on the opposite side of the chamber is used to characterise the transitions we want to work with. Adding the mirror allows us to cool down the atoms and characterise the cooling of the atoms. The 401 nm laser, which is normally responsible for the Zeeman slower, transversal cooling and imaging, is in this case necessary to align the 741/841 nm lasers to make sure that all the lasers hit the atom cloud in the chamber. Figure modified from Ref. [43].

In addition, to improve the cooling, we added an electronic setup to interleave the cooling light with the ODT light. The idea is that the energy levels of an atom in the ODT are affected by the AC Stark shift. This means that in general levels get shifted and split, shifting and inhomogeneously broadening the resonance condition for the cooling light. This reduces the total efficiency of the cooling. A simple solution to this problem is the so-called strobing technique. Strobing is a rather easy-implied and powerful technique to prevent the presence of AC Stark shifts. However, it is done by switching off the ODT by externally modulating the RF to the AOM of the ODT for not too long. Therefore, we use switches to chop the beam at 10 kHz for an 80 % duty cycle (80 % on, 20 % off). While the ODT is off, the narrow-line lasers are switched on, cooling the atoms. It is important to mention that the strobing frequency has to be larger than the ODT frequency, but small enough so that the time while the ODT is off is long enough to scatter enough photons from the cooling light to have sufficient cooling. Fig. 9 shows the sequence of the experiment and

when the strobing is applied. The duration of the cooling time and the time before imaging can be varied for each measurement.

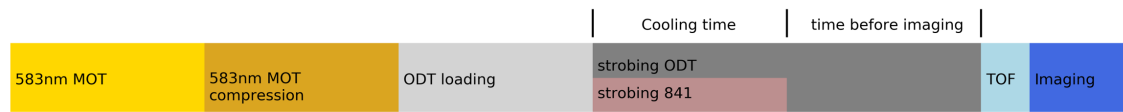


Figure 9: A rough schedule of the sequence of the experiment. The experiment starts by creating the 583 nm MOT. After that step the atoms get compressed till we reach temperatures as low as $\sim 10 \mu\text{K}$. The next step is to load the atoms into the ODT for evaporative cooling to quantum degeneracy. Then we strobe the ODT as well as the 841 nm laser for the duration of the cooling time and the time before the imaging. These two values vary depending on the measurement. After the strobing follows the Time-of-Flight (TOF) and after that the imaging.

4 Cavity Setup

Cavities are commonly used in experimental physics to stabilise the optical frequency of a laser to the frequency of a resonance of the reference cavity, and to narrow down the linewidth of the light compared to a free-running laser. One main part of the setup is a Stable Laser Systems (SLS) cavity, which is necessary, since we want to work with very narrow transitions. While the linewidth of a grating-stabilised diode laser is typically in a range of a few MHz broad, we want to be able to narrow it down to the natural linewidths of the corresponding atomic transitions, having 2 kHz and 8 kHz (see Tab. 2). This chapter consists of four sections, where the first section summarises the basic concepts of cavity physics, followed by the main properties of the cavity used for this project. The third section focusses on the locking technique we use in this project, and lastly, a cavity characterisation is presented.

4.1 Theoretical Basics of Cavity Physics

In this chapter we consider a cavity of length L , consisting of two identical, semipermeable mirrors. Furthermore, we consider an incoming monochromatic wave $E_{\text{in}} = E_0 e^{i\omega t}$, where ω denotes the laser frequency and E_0 the complex amplitude. The light passes through both cavity mirrors, which have a reflexion coefficient r and a transmission coefficient t . Assuming that the absorption of the light at the mirrors is negligible, the relation between these two coefficients can be described as

$$r^2 + t^2 = 1. \quad (15)$$

In addition, each reflexion leads to a shift of the electric field's phase $\Delta\phi$, which can be described as

$$\Delta\phi = \omega \cdot \frac{(n+1)L}{c}, \quad (16)$$

with n being the refractive index of the medium between the cavity, which in this case is vacuum ($n = 1$). Furthermore, the total reflected light field E_{ref} can be obtained by summing up the partially reflected field as

$$E_{\text{ref}} = E_{\text{in}} \cdot (-r + t^2 r e^{i\Delta\phi} + t^2 r^3 e^{i2\Delta\phi} + \dots). \quad (17)$$

The transmitted field E_{trans} can be calculated analogically, by summing up the partially transmitted field. Taking the absolute square of the reflected field, the

total reflected light intensity I_{ref} can be determined as:

$$I_{\text{ref}} = I_{\text{in}} \cdot \frac{4R \sin^2(\Delta\phi)}{T^2 + 4R \sin^2(\Delta\phi/2)}. \quad (18)$$

Respectively, the transmitted intensity I_{trans} can be calculated as:

$$I_{\text{trans}} = I_{\text{in}} - I_{\text{ref}} = I_{\text{in}} \cdot \frac{T^2}{T^2 + 4R \sin^2(\Delta\phi/2)}, \quad (19)$$

where I_{in} denotes the incoming intensity defined as $I_{\text{in}}^2 = \frac{\epsilon_0}{2} c \cdot E_{\text{in}}^2$ with ϵ_0 being the electric constant, $R = r^2$ the reflectance and $T = t^2$ the transmission of the mirrors. Furthermore, an important parameter to characterise a cavity is the so-called free spectral range (FSR), which defines the distance in frequency between two transmitted or reflected intensity maxima, which are also known as cavity modes. This spacing can be obtained by the equation

$$\text{FSR} = \frac{c}{2L}. \quad (20)$$

An additional important parameter is the full width at half maximum (FWHM) of a mode, which defines the linewidth Γ of a transmission or reflexion peak. A relation of these two parameters can lead to another parameter that is crucial to characterise a cavity, namely the finesse \mathcal{F} . This can be expressed by the ratio of the FSR and the FWHM,

$$\mathcal{F} = \frac{\text{FSR}}{\text{FWHM}} = \frac{\text{FSR}}{\Gamma}. \quad (21)$$

Assuming that we have low losses in the cavity and high reflectivity, another way to calculate the finesse is by regarding the reflectance of the mirrors, leading to the following equation:

$$\mathcal{F} \approx \frac{\pi\sqrt{R}}{1-R}. \quad (22)$$

Additionally, knowing the linewidth of the cavity, the average storage time τ_{p} - also known as photon lifetime- can be determined with the aid of the relation:

$$\tau_{\text{p}} = \frac{1}{2\pi\Gamma}. \quad (23)$$

Fig. 10 shows the function that describes the transmission through a cavity, also known as transversal electromagnetic modes TEM_{nm} [48–50]. The quantum num-

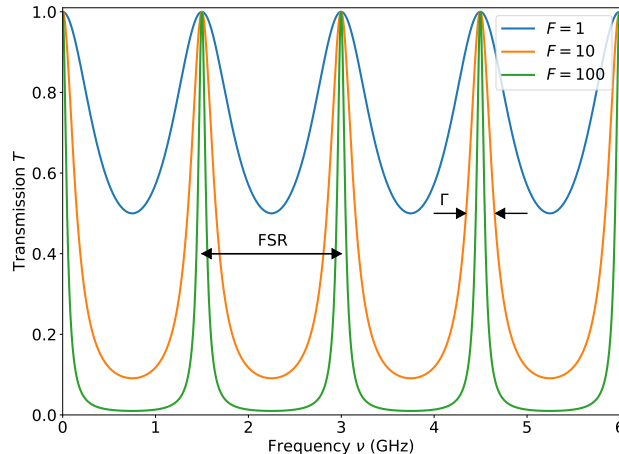


Figure 10: The transmitted spectrum in dependence of the frequency is plotted for three different values of the finesse $\mathcal{F} = 1$, $\mathcal{F} = 10$ and $\mathcal{F} = 100$. In addition, the free spectral range FSR as well as the linewidth Γ are marked with the black arrows.

bers n and m correspond to positive integers, which describe the knots of the electric field force transversely to the propagation direction. The transmission frequency of the modes depends on the geometry of the cavity, such as the length and curvature of the mirrors. To achieve good locking performance, we have to eliminate the higher TEM modes near the TEM₀₀ mode, which is also known as the Gaussian mode. If we have more TEM modes near the TEM₀₀, such as the TEM₀₁ or the TEM₁₀ mode, then our locking can jump in these modes instead of staying in the TEM₀₀ mode. To avoid this issue we have to achieve a good cavity coupling, meaning that on the transmission spectrum we ideally see only the TEM₀₀ mode.

Assuming that our cavity consists of a plane mirror and a curved mirror, the frequency distance between two TEM_{nm} modes can be calculated by the following equation:

$$\delta_\nu = \frac{c}{2L}(n+m+1) \frac{1}{\pi \cos\left(\sqrt{1 - \frac{L}{\rho}}\right)}, \quad (24)$$

where ρ denotes the mirror curvature. For a good cavity coupling, it is crucial that the laser beam propagation axis equals the axis of the mirrors and the intensity profiles of the beam have to be spatially well overlapped. Furthermore, the wavefront of the beam has to match the radius of the mirrors, also known as mode matching. This can be done by focussing a laser beam into a cavity with the aid of optical elements such as lenses or curved mirrors. According to the mode matching conditions

and the assumed cavity geometry, the beam waist has to be

$$w = \sqrt{\left(\frac{\lambda L}{\pi} \sqrt{\frac{\rho - L}{L}}\right)}, \quad (25)$$

where λ denotes the wavelength. For our cavity parameters, $L = 10$ cm and $\rho = 500$ mm, we obtain for $\lambda = 741$ nm a beam waist of $w = 217 \mu\text{m}$ and for $\lambda = 841$ nm a beam waist of $w = 231 \mu\text{m}$.

4.2 Stable Laser Systems (SLS) Cavity

The cavity is a crucial part of this setup because we are aiming for narrow transitions. Since the linewidths of the cooling transitions are 1.78 kHz for Dy and 8.0 kHz for Er, we have to lock the lasers to stable frequency references. We used a cavity from Stable Laser Systems, which is a cylinder cavity with a length of 100 mm and a diameter of 50 mm, as shown in the photo on the left in Fig. 11.

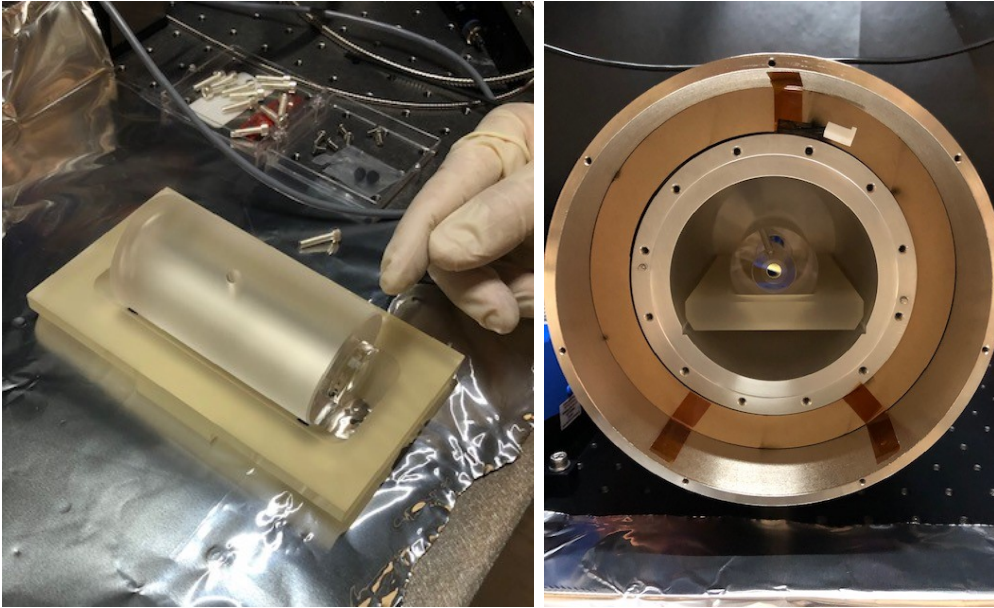


Figure 11: The left picture shows the cavity with a length of $L = 10$ cm and a diameter of 50 mm. The photo on the right shows the cavity in the cavity housing before the lid was screwed on. This process had to be carried out with care to not alter the quality of the mirrors and the position of the cavity after placing the lid.

The cavity consists of one plain mirror and one concave mirror with a radius of 500 mm. With these parameters, the free spectral range can be calculated with the following equation $\nu_{\text{FSR}} = \frac{c}{2L}$. Here, c represents the speed of light and L the

length of the cavity, leading to a free spectral range of 1.49 GHz. According to the specifications, the cavity has a target finesse in the range of 10000 – 50 000 at 583 – 841 nm. The resonator is surrounded by an outer shell, as shown in the right picture in Fig. 11, with thermal insulation, heaters, and thermistors.

After assembling the cavity, the next step was to prepare it by connecting a TiTan ion pump⁶ and a PID⁷. A stable temperature is crucial since a temperature change would affect the distance of the mirrors, leading to a drift in frequency. For the initial pumpdown, an external pumping station was attached until the pressure stabilised at a value of 1.3×10^{-7} mbar and the PID regulated the temperature at 34.25(5) °C.

4.3 Pound-Drever-Hall (PDH) locking technique

There are several techniques to stabilise the frequency of a laser. In this project we are using the Pound-Drever-Hall locking technique, which belongs to one of the most commonly employed and powerful active laser stabilisation techniques. This technique requires a high-finesse cavity to lock the frequency of the laser on the cavity's resonance. The idea behind this technique is to measure the frequency of the laser with the aid of an optical resonator and feed back the measurement to the laser in order to suppress frequency fluctuations. The light gets modulated by an EOM, which creates sidebands on the laser frequency separated by the modulation frequency. When the main frequency component is resonant with the cavity, those sidebands are reflected. This reflected signal can be used to generate the error signal for laser lock [51]. In addition, this technique is suitable for this project, since we are focussing on two atomic species and the cavity can be chosen to work for a specific wavelength range. However, for instance stabilising the frequency with an atomic vapour cell would require one cell for each element.

The idea for the PDH frequency stabilisation is to use the derivative of the reflected intensity instead of the intensity itself to get an error signal for the laser locking. After having a clear error signal, we use this to adjust the laser frequency onto the cavity resonance. This can be achieved by means of a servo loop, where a commonly used servo is a PID device. A PID transforms an input by a proportional, an integral, and a derivative component and outputs a feedback signal. The proportional term depends on the difference between the set-point and the process variable. It determines the ratio of the output response to the error signal. The integral compo-

⁶Gamma Vacuum TiTan™ Ion Pump

⁷Temperature Controller, LFI-3751

ment sums the error term over time, and the derivative response is proportional to the rate of change of the process variable. However, for laser stabilisation, only a PI loop is used because a laser responds fast enough, when adjusting the frequency [52]. Thus, adjusting the frequency can be done by varying the frequency and observing the response of the reflected beam. Above resonance, the derivative of the reflected intensity with respect to the laser frequency is positive, and below resonance the derivative negative. In addition, if we are above resonance and the frequency of the laser is varied sinusoidally over a small range, the reflected intensity also varies sinusoidally and in phase with the modulation frequency. Below resonance, the reflected intensity is at a minimum and will vary by π out of phase from the frequency. The measurement of the derivative of the reflected intensity can be fed back to the laser to keep the frequency constant. In addition, the reflected signal consists of the beam that never enters the cavity because it is already reflected at the first mirror of the cavity, and the light transmitted back after some storage time in the cavity. The two contributions to the signal measured by a photodiode observing the reflected beam with intensity I_{ref} (Eq.(18)) at resonance are exactly phase shifted by π and interfere destructively.

To modulate the phase of the laser beam we use an EOM with a modulation frequency of Ω and a modulation depth of β . The resulting light field is of the form

$$E_{\text{in}} = E_0 \exp(i(\omega t + \beta \sin(\Omega t))) = E_0 \sum_n J_n(\beta) \exp(i(\omega - n\Omega)t). \quad (26)$$

Here, the Fourier expansion can be written in terms of Bessel functions $J_n(\beta)$. For small modulation depths, the light field can be approximated as

$$E_{\text{in}} = E_0 \exp(i\omega t)(-J_1(\beta) \exp(-i\Omega t) + J_0(\beta) + J_1 \exp(i\Omega t)). \quad (27)$$

By looking at this expression, one can see that the light field consists of three different terms oscillating at different frequencies. The term oscillating at frequency ω describes the so-called carrier wave. The other two terms oscillating at $\omega - \Omega$ and $\omega + \Omega$ describe the sidebands. The relative intensities of the carrier wave and the sidebands correspond to the value of the Bessel functions. To obtain the signal from the reflected intensity, the terms in Eq.(27) need to be multiplied with the reflexion coefficient, which is defined as

$$F(\omega) = \frac{r \left(\exp i \frac{\omega}{FSR} \right) - 1}{1 - r^2 \exp \left(i \frac{\omega}{FSR} \right)}. \quad (28)$$

In the PDH setup, this leads to a total intensity of the reflected beam, which is given by

$$E_{\text{ref}} = E_0 [-F(\omega - \Omega)J_1(\beta) \exp(-i\Omega t) + F(\omega)J_0(\beta) + F(\omega + \Omega)J_1(\beta) \exp(i\Omega t)]. \quad (29)$$

As the signal measured with the photodiode corresponds to the intensity given by $|E_{\text{ref}}|^2$, the measured signal $S(\Delta_\nu, \phi)$ is given by

$$S = C + A \cdot \frac{\Gamma \Delta_\nu \Omega (\sin \phi \cdot \Gamma (\Gamma^2 + \Delta_\nu^2 + \Omega^2) + \cos \phi \cdot \Omega (\Gamma^2 - \Delta_\nu^2 + \Omega^2))}{(\Gamma^2 + \Delta_\nu^2) \cdot (\Gamma^2 + (\Delta_\nu + \Omega)^2) \cdot (\Gamma^2 + (\Delta_\nu - \Omega)^2)}. \quad (30)$$

Here, the parameter C describes the offset, A the amplitude, Ω the modulation frequency, Γ the linewidth, ϕ the phase offset, and Δ_ν the detuning, which is defined as $\Delta_\nu = \Delta - \Delta_0$, where Δ_0 denotes the zero crossing of the error signal. The influence of the phase and the linewidth of the cavity on the error signal is shown in Fig. 12.

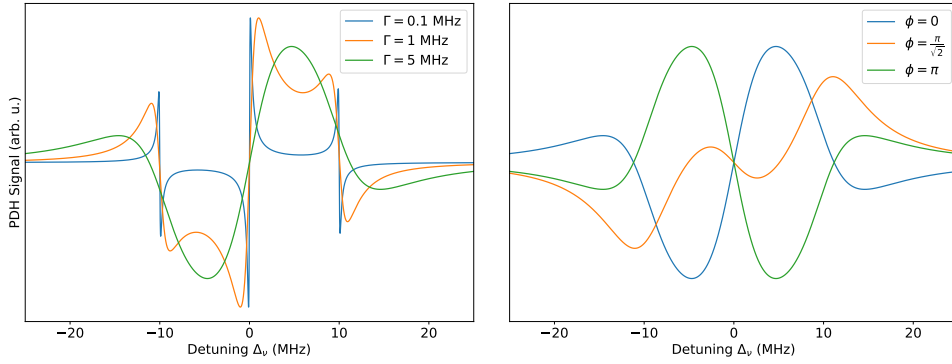


Figure 12: Error signal for different linewidths Γ of the cavity and different phases ϕ as a function of the detuning Δ_ν from the resonance. The left plot shows the PDH error signal for the linewidths of 0.1 MHz (blue line), 1 MHz (orange line) and for 5 MHz (green line). The right plot shows the influence of the phase ϕ on the error signal for the three different phases 0 (blue line), $\pi/\sqrt{2}$ (orange line) and π (green line).

If we are working with slow modulation, that is, a low frequency, which is far away from cavity resonance, the standing wave inside the cavity is always in equilibrium with the incident beam, and all the light is reflected from the cavity. This leads to an error signal without sidebands. On the other hand, if the carrier is near resonance and the modulation frequency is high enough, then we get an error signal with sidebands and the reflexion coefficient depends on the cavity's resonant frequency. In our case, we are working with fast modulation since we have such narrow linewidths and want fast relocking. In addition, the tunable diode lasers we are working with

can be tuned with a digital controller called DLC pro from TOPTICA. With that we use the digitally controlled fast laser locking module, called Fast Analog Linewidth Control (FALC) pro. The FALC pro is a high-speed linear control amplifier, which is designed for laser frequency stabilisation and is compatible with the PDH locking technique. Additionally, due to its high speed regulator consisting of three integrating and two differentiating parameters, this module enables working with ultra-narrow transitions.

Fig. 13 shows a schematic setup of the electronics needed for the PDH locking.

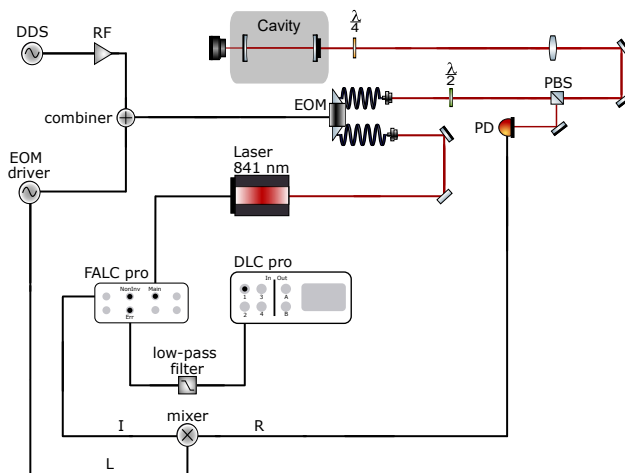


Figure 13: Schematic setup of the electronics needed for the PDH locking technique based on the actual setup of the project. This technique stabilises the laser frequency with the aid of an error signal, which is generated from the system and is transformed into a feedback signal by means of a servo. The PDH signal is created by modulating (EOM) the laser beam and imprinting sidebands at the modulating frequency. The light passes through the cavity, and the reflexion is separated from the incoming beam with the aid of the PBS and the $\lambda/4$ -plate. Then the reflexion gets detected by a PD. The error signal gets obtained and mixed with the signal of an EOM driver, which passes through the FALC pro and is sent as a feedback signal back into the laser.

The PDH signal is generated by modulating (EOM) the laser beam and imprinting sidebands at the modulating frequency. After the light passes through the cavity, a PBS and a quarter-wave plate separate the incoming and the reflected beam. The reflexion is detected by the PD, which is connected to a mixer. The error signal is mixed with the signal of the EOM driver and is fed back to the laser through the FALC pro. The signal to the EOM is combined by a DDS and the mixed signal from the EOM driver. In our case, the mixer and the EOM driver are combined in a single module.

4.4 Cavity Characterisation

In the following chapter, a short analysis has been done to characterise the cavity after assembling and check the finesse \mathcal{F} , the linewidth, and the storage time τ_p for both lasers. This part was done before tuning the lasers to a specific frequency. The setup used for these measurements is shown in Fig. 6. All results are calculated as an average over several error signals.

4.4.1 PDH Signal

In order to determine the finesse, six measurements of the PDH error signal for each laser were recorded with the aid of an oscilloscope, as shown in Fig. 14. The turquoise line shows the PDH signal and the pink line shows the transmission signal, which is detected at the photodiode. The orange line is the sweeping signal and is used to trigger the signals.

To have good locking conditions, the alignment into the cavity has to be done carefully to have a signal with as few modes as possible. The alignment can be improved by observing the transmitted intensity at the end of the cavity with a photodiode and an oscilloscope and walking the beam so that the transmission of the TEM_{00} mode is as high as possible and no other modes are visible.

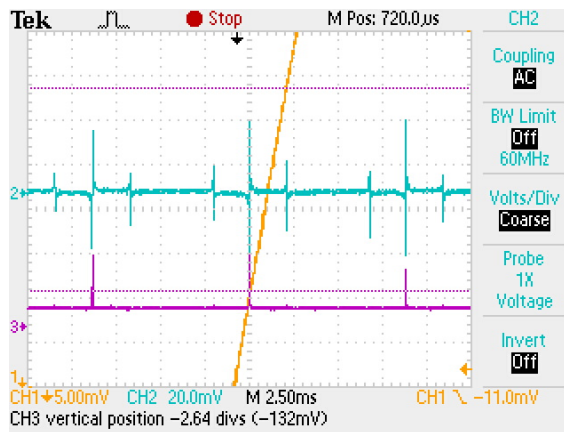


Figure 14: Screenshot of the oscilloscope, where the error signal (turquoise) and the transmission (pink) of the laser frequency with the imprinted sidebands are obtained. On the y-axis we have the voltage depending on the detuning on the x-axis. The orange line is the sweeping signal and is used as a trigger.

The PDH signals of both lasers are then fitted to Eq. (30) as shown in Fig. 15, by which the linewidth can be determined. These plots represent one of the six recorded signals.

Furthermore, knowing that the free spectral range of the cavity corresponds to

FSR = 1.49 MHz, the finesse \mathcal{F} can be calculated with Eq. (21) as well as the storage time τ_p with Eq. (23). The results, which are the average over the six measurements, are given in Tab. 3. The large uncertainties can be explained by the outliers of the signals, which can be seen in both plots in Fig. 15 and are caused by the signal shifts. According to the information of the ordered cavity, the targeted finesse should be in the range of 10000 to 50000, which is in line with our measurements.

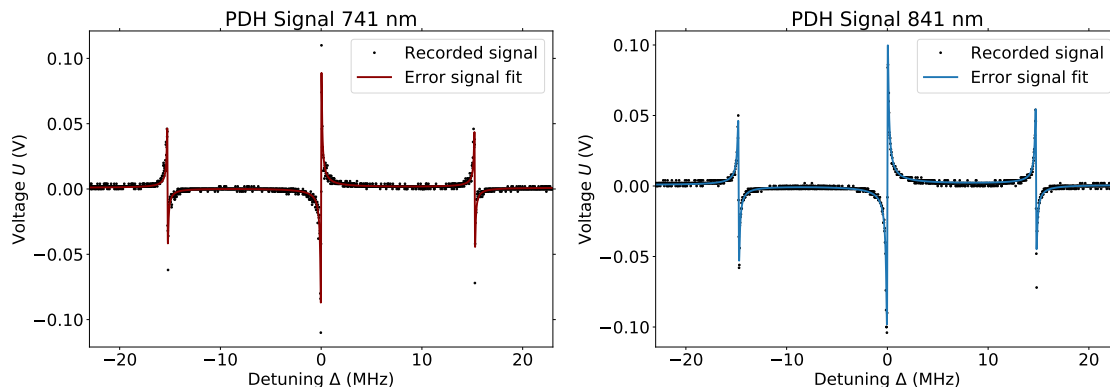


Figure 15: The PDH error signal of both lasers 741/841 nm as a function of the voltage depending on the detuning. The signals are fitted with the Eq. (30) in order to obtain the linewidth Γ and calculate further parameters such as the finesse \mathcal{F} and the photon lifetime τ_p of the cavity. The outliers seen here could be caused by the movement of the signal.

Table 3: Results of the fitted finesse, as well as the measured finesse and photon storage according to the recorded signals in Fig. 15.

	Linewidth Γ (kHz)	Finesse \mathcal{F}	storage time τ_p (μ s)
741 nm	46.3(7)	32300(500)	6.9(1)
841 nm	51.9(3)	28920(190)	6.14(4)

4.4.2 Cavity Ring-Down

A second method to calculate the finesse is by performing so-called cavity ring-down measurements. The storage time of the light in the cavity can be used to calculate the finesse, which is determined by the decay time. For the measurement, the frequency of the laser is shifted away from resonance as fast as possible, and the subsequent decay of light out of the cavity is measured. Fitting the exponential decay with a fit of the form $f(t) = C + A \cdot e^{-\frac{t}{\tau_p}}$, where C is the offset and A the

amplitude, as shown in Fig. 16 the storage time τ_p can be extracted. The results were averaged over approximately six measurements for the smallest possible gain of the photodiode. For the laser at 741 nm, the process was conducted with a gain of 30 dB. The photodiode was fast enough to detect the 841 nm laser with a gain of 10 dB. The plots in Fig. 16 show one of the few measurements that were recorded. Further, the average of the lifetime was calculated and by knowing the relation between the resonance linewidth and the photon lifetime [49]:

$$\Gamma = \frac{1}{2\pi\tau_p}, \quad (31)$$

the linewidth can be determined and then the finesse. For the 741 nm laser, the average photon lifetime is $\tau_p = 1.708(3) \mu\text{s}$ leading to a linewidth of $\Gamma = 94.0(2) \text{ kHz}$.

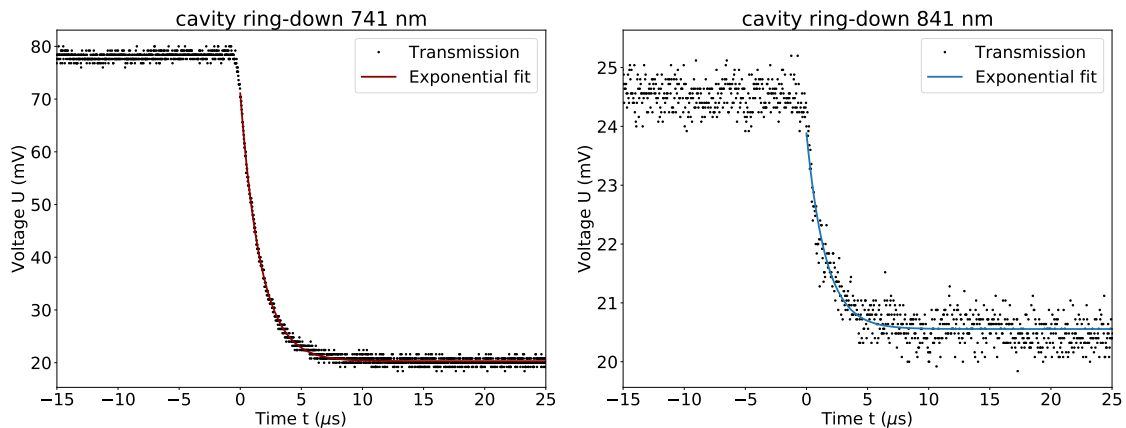


Figure 16: Cavity ring-down measurements for both 741/841 nm lasers. The black dots represent the recorded data points from the transmission and the lines are an exponential fit of the form $f(t) = C + A \cdot e^{-\frac{t}{\tau_p}}$. For the 741 nm laser a finesse of a value $\mathcal{F} = 15853(31)$ is extracted, whereas for the 841 nm laser the value is $\mathcal{F} = 16630(270)$.

Table 4: Results of the fitted finesse, as well as the measured finesse and photon storage according to the recorded signals in Fig. 16.

	Linewidth Γ (kHz)	Finesse \mathcal{F}	storage time τ_p (μs)
741 nm	94.0(2)	15853(31)	1.708(3)
841 nm	89.6(9)	16630(270)	1.78(3)

Hence, the finesse is $\mathcal{F} = 15853(31)$. Accordingly, for 841 nm the photon lifetime is $\tau_p = 1.78(3) \mu\text{s}$ and the linewidth $\Gamma = 89.6(9) \text{ kHz}$, corresponding to the finesse of

the value $\mathcal{F} = 16\,630(270)$. The results are listed in Tab. 4. Comparing both finesse values from Tab. 3 and Tab. 4 with the expected value of the cavity range, both values are in the estimated range. However, a cavity-ring-down measurement should probably lead to more reliable results of the finesse, since the exponential fit involves fewer fit parameters compared to Eq. (30). In addition, in this measurement, we measure how fast the light decays in the cavity instead of an error signal, leading to a more direct measurement.

5 Transition characterisation

There are several atomic transitions in erbium and dysprosium as shown in their energy spectra in Fig. 2 and aiming to work with a specific transition can sometimes be tricky. There are many factors that can affect the measurement such as photoassociation leading to another transition, broadening mechanisms causing a broader linewidth than expected, or even systematic uncertainties such as calibrations, and so on. Therefore, a transition has to be characterised and compared with literature values to ensure that it is the right one.

In the following chapter, we focus on the 841 nm transition of erbium and specify the method we used to find the transition as well as its characterisation. Furthermore, parameters such as the g -factor, the linewidth, and its broadening have been determined and compared to the expected values.

By knowing the wavenumber k of the $4f^{11}(^4I_{15/2}^o)5d_{5/2}6s^2(15/2, 5/2)_7^o$ transition (see Tab. 2), which is at $11\,887.503\text{ cm}^{-1}$ according to NIST [37] and corresponds to the transition at 841 nm, one can calculate its exact wavelength. The wavenumber defines the reciprocal of the wavelength λ of the wave and describes how many wavelengths fit into a unit of distance. The relation between these two parameters is $\lambda = \frac{1}{k}$ and leads, for our wavenumber, to the wavelength of 841.219 56 nm. Given the narrow linewidth, the precision of this value still means that we have to look for our transition in a range around it. Tuning the frequency can be achieved by scanning the piezo voltage. A grating inside the laser head, which is used for frequency tuning, is mounted on a piezo. Thus, by changing the piezo voltage the grating can be rotated, leading to a frequency change. The transition we are expecting should have the following properties as listed in Tab. 5.

Table 5: Important parameters of the Er transition at 841.22 nm are listed such as the linewidth Γ , the lifetime τ , the natural linewidth $\Delta\nu$, the saturation intensity I_{sat} , the Doppler temperature T_{Doppler} , the recoil temperature T_{recoil} [37] and the Landé-Faktor g [34].

Transition	Γ	τ	$\Delta\nu$	I_{sat}	T_{Doppler}	T_{recoil}	g -factor
841.22 nm	$5.0 \times 10^4\text{ s}^{-1}$	$20 \pm 4\ \mu\text{s}$	8.0 kHz	18 mWm^{-2}	190 nK	81 nK	1.153

We did a scan between 841.2253–841.2238 nm and found a transition at 841.2250 nm according to the wavemeter as shown in Fig. 17(a). The uncertainty of the position of the transition could be based on the calibration of the wavemeter.

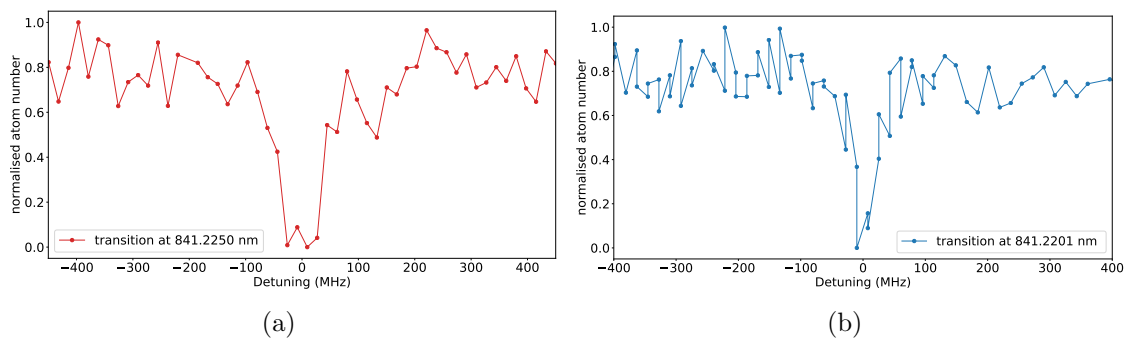


Figure 17: Scans of the two transitions that were discovered around the wavelength of 841.21956 nm. Both plots show the transitions as a normalised loss feature depending on the detuning, whereas the transition are centred to be the origin. Though one transition was found at a wavelength of 841.2250 nm and the other at 841.2201 nm, the shifted position of the wavelength can be argued by the calibration of the wavemeter. Furthermore, a superficial analysis has shown that the transition in (b) does not fit to the expected values of Tab.5 and hence the detailed analysis is focused on the transition in (a).

In a second scan between the range 841.2205 – 841.2187 nm, we discovered a second transition at wavelength 841.2201 nm as shown in Fig. 17(b). However, after some superficial analysis, it turned out that the transition did not match to the transition we were looking for. This transition could possibly be caused by photoassociation since it is only a few nanometres away from the other transition we have found, and it cannot be another erbium transition according to its energy spectrum. Therefore, the analysis is focused on the first transition at 841.2250 nm.

If we searched for the Dy transition, we would focus on the $4f^9(6H^{\circ})5d6s^2\ ^7K_9^{\circ}$ transition at a level of $13\,495.92\text{ cm}^{-1}$ according to NIST [34] leading to an exact wavelength of 740.96468 nm with the properties listed in Tab. 6.

Table 6: Important parameters of the Dy transition at 740.96 nm are listed such as the linewidth Γ , the lifetime τ , the natural linewidth $\Delta\nu$, the saturation intensity I_{sat} , the Doppler temperature T_{Doppler} , the recoil temperature T_{recoil} [7] and the Landé-Faktor g [34].

Transition	Γ	τ	$\Delta\nu$	I_{sat}	T_{Doppler}	T_{recoil}	g -factor
740.96 nm	$1.12 \times 10^4\text{ s}^{-1}$	$89.3\ \mu\text{s}$	1.78 kHz	5.7 mWm^{-2}	42.7 nK	213 nK	1.23

5.1 Linewidth measurement and broadening mechanisms

The first parameter that we want to determine is the linewidth of the transition. Tab. 5 shows that the expected natural linewidth should be 8 kHz [37]. In order to observe the natural linewidth, we perform atom loss spectroscopy. In this case, we load an atom cloud into the optical dipole trap and evaporatively cool the atoms down to about 6 μ K. Furthermore, we shine the 841 nm light onto the cloud, which the atoms absorb, leading to heating. Therefore, we lose atoms from the trap and observe atom loss. By observing the atom number depending on the detuning of the laser from resonance, we can see a dip which indicates our transition.

Observing a transition in an experiment leads to broader results, as expected. This broadening can be explained by various broadening mechanisms. In this case, we also obtain different broadening mechanisms such as Doppler, Power and pressure broadening leading to a broader linewidth as expected in comparison to the natural linewidth of the transition.

Natural linewidth

The natural linewidth $\Delta\nu$ is defined as the fundamental limit of the linewidth, which depends on the lifetime τ of the excited state leading to the following relation:

$$\Delta\nu = \frac{\Delta E}{h} = \frac{1}{2\pi\tau}. \quad (32)$$

Furthermore, the natural linewidth can be described with the aid of a classical model of a damped harmonic oscillator, leading to a Lorentzian function of the form:

$$f(\nu) = \frac{A}{2\pi} \cdot \frac{\Delta\nu}{(\nu - \nu_0)^2 + (\Delta\nu/2)^2}. \quad (33)$$

Here, A is the normalisation factor, ν the frequency, ν_0 the central position of the peak and $\Delta\nu$ the natural linewidth of the transition.

Doppler broadening

Doppler broadening is caused by the Doppler effect which describes a frequency shift when the atoms are moving toward or away from the detector [36, 49]. Therefore, for atoms that emit radiation with frequency ν_0 and move with a velocity v , the

detector detects radiation with frequency:

$$\nu = \nu_0 \left(1 \pm \frac{v}{c}\right). \quad (34)$$

Since the atoms in an atom cloud move randomly in all directions the detector sees a Doppler-broadened spectral line profile, which can be described by the Boltzmann distribution as:

$$n(v)dv = \sqrt{\frac{2k_{\text{B}}T}{m\pi}} \cdot \exp\left(-\frac{mv^2}{2k_{\text{B}}T}\right)dv. \quad (35)$$

Here m is the mass of the particles, T the temperature of the gas, and k_{B} the Boltzmann constant. The full width at half maximum of the distribution is known as the Doppler width and leads to the following relation [36, 49]:

$$\Delta\nu_{\text{D}} = 2\sqrt{\ln 2} \cdot \frac{1}{\lambda} \cdot \sqrt{2k_{\text{B}}T/m}. \quad (36)$$

Power- and saturation broadening

Power and saturation broadening are two additional mechanisms, which increase the linewidth of the transition. They occur when an atomic absorption line is driven by a steady light source. The broadening is then caused by the (partial) saturation of the transition caused by the light intensity. This effect has a Lorentzian line shape with a full width half-maximum of the form:

$$\Delta\nu_{\text{P}} = 2\pi \cdot \Delta\nu (1 + s)^{1/2}, \quad (37)$$

where $\Delta\nu$ is the natural linewidth, s is the saturation parameter and is defined as $s = \frac{I}{I_{\text{sat}}}$. The peak intensity I for a Gaussian beam is defined as $I = \frac{2P}{\pi\omega^2}$, with P being the optical power and ω the radius of the Gaussian beam. Furthermore, I_{sat} is the saturation intensity, which for the 841 nm erbium transition is $I_{\text{sat}} = 18 \text{ mW/m}^2$ [37].

Further broadening mechanisms

Further examples of broadening are collisional or pressure broadenings, which are caused by atom-atom collisions leading to a shifted transition frequency and therefore to broadening. This effect is described by a Lorentzian shape with FWHM of the following form:

$$\Delta\nu_{\text{col}} = n\sigma_{\text{cs}}v \propto n\sqrt{T}, \quad (38)$$

where σ_{cs} indicated the collision cross-section, and the velocity v is defined as $v = \sqrt{2k_B T/m}$.

In an experiment, the linewidth of a transition will be affected by several broadening mechanisms simultaneously. If the broadening that occurs is described by both a Lorentzian and a Gaussian function, then the line shape can be represented by a convolution of both line shapes leading to the so called Voigt, which has the following form:

$$V(\nu; \Delta\nu_G, \Delta\nu_L) = \int_{-\infty}^{+\infty} G(\nu'; \Delta\nu_G) L(\nu - \nu'; \Delta\nu_L) d\nu'. \quad (39)$$

Here $G(\nu'; \Delta\nu_G)$ represents the Gaussian profile and $L(\nu - \nu'; \Delta\nu_L)$ the Lorentzian profile.

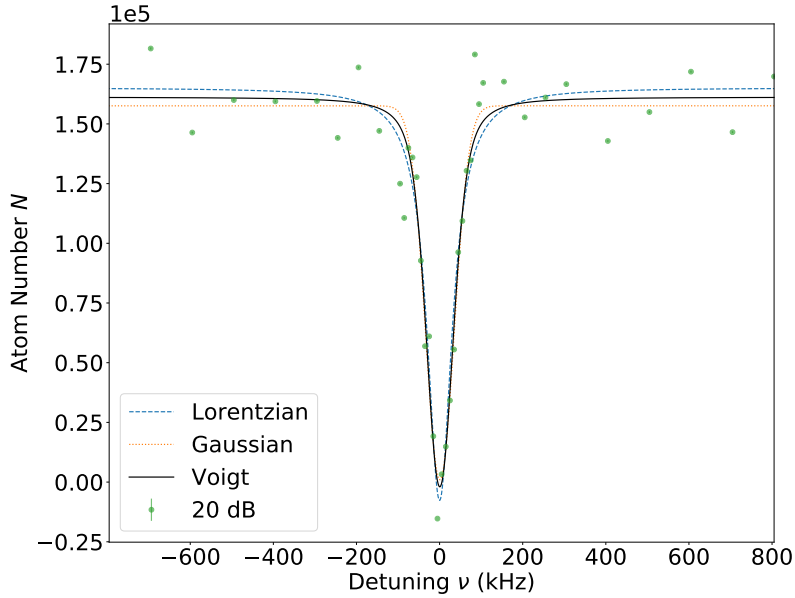


Figure 18: Atom loss spectroscopy at an attenuation of 20 dB. The plot shows the atom number depending on the detuning. The data points are fitted with a Lorentzian, a Gaussian and a Voigt function in order to compare the fits and find the most suitable fit function. This step has been done for seven different attenuations. In all cases, the chi-square χ^2 is determined and compared, showing that the Voigt function leads to the most suitable fits. The results are listed in Tab. 10 in Appendix A.

Fig. 18 shows as an example the recorded data points for the 841 nm transition with an attenuation of 20 dB fitted by a Gaussian, a Lorentzian, and a Voigt function. Furthermore, the linewidth of each fit as well as the chi-square value χ^2 has been determined for seven different attenuations in a range of 0 – 30 dB and are listed in Tab. 10 in Appendix A. The comparison of the values led to the Voigt function being

the most suitable fit for the transitions. Hence, Fig. 19 shows the data points and the Voigt fit for four different attenuations, whereas all the transitions are centred with respect to the 30 dB transition. All the fit parameters such as the offset C , the amplitude A , the central position ν_0 and the corresponding power P as well as the attenuation can be found in Tab. 7. Furthermore, in this plot the data points are averaged over around 5-6 recorded data points (around 6 data points were recorded around the dip and 4 on the sides); however, the error is so low that it cannot be seen. The data points are centred with respect to the centre position of the red curve which corresponds to an attenuation of 30 dB. Therefore, the detuning is represented on the x-axis. In addition, the plot shows that for attenuations 0 dB and 10 dB the transition is oversaturated, i.e., all atoms are lost near the resonance. The measurement at 20 dB avoids this saturation effect, leading to the narrowest value with a Gaussian width of 29(8) kHz and a Lorentzian width of 18 ± 10 kHz, with a centre position at 569.70(2) MHz. Increasing the attenuation to 30 dB leads to a wider transition with a Gaussian linewidth of 35 ± 19 kHz and a Lorentzian linewidth of 0 ± 27 kHz at $\nu_0 = 569.70(5)$ MHz, which shows that the Lorentzian fit could not be found for this transition. Further, for the transition at 30 dB we observe more outliers, which could be explained by laser noise.

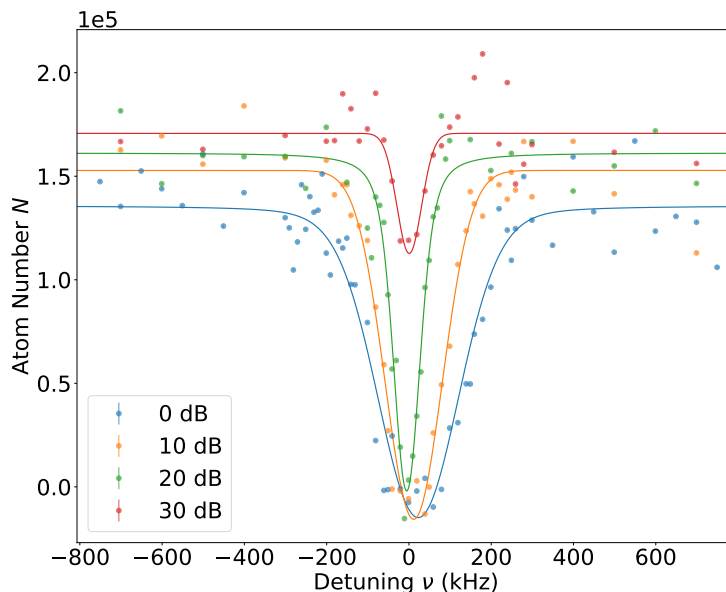


Figure 19: Atom loss spectroscopy for four different attenuations and fitted by a Voigt function of the form of Eq. (39). The plot shows the atom number depending on the detuning. In this plot the transitions are centred in respect to the centre of the red curve which corresponds to an attenuation of 30 dB. In addition, the data points are fitted with a Lorentzian function of the form Eq. (33). The corresponding results of the parameters are listed in Tab. 7.

Table 7: Parameters of the fitted Lorentzian Eq. (33) for the four different attenuations shown in Fig. 19 and for three additional attenuations. The parameters listed are offset C , normalisation factor A , central position of the peak ν_0 and natural linewidth of the transition $\Delta\nu$.

Att. (dB)	P (μW)	C (atoms)	A (atoms \cdot Hz)	ν_0 (MHz)	$\Delta\nu_G$ (kHz)	$\Delta\nu_L$ (kHz)
0	2.03(6)	$1.36(5) \times 10^5$	$-4.0(6) \times 10^7$	569.72(4)	108(23)	20 ± 40
5	1.25(4)	$1.62(7) \times 10^5$	$-4.0(8) \times 10^7$	569.71(4)	78 ± 23	30 ± 40
10	0.75(2)	$1.53(5) \times 10^5$	$-2.9(4) \times 10^7$	569.71(2)	82(1)	0 ± 22
15	0.40(1)	$1.67(3) \times 10^5$	$-2.6(3) \times 10^7$	569.70(2)	47(9)	21 ± 12
20	0.25(8)	$1.61(4) \times 10^5$	$-1.6(2) \times 10^7$	569.70(2)	29(8)	18 ± 10
25	0.18(5)	$1.62(3) \times 10^5$	$-9(1) \times 10^6$	569.70(2)	34(8)	11 ± 22
30	0.15(4)	$1.71(3) \times 10^5$	$-4(2) \times 10^6$	569.70(5)	35 ± 19	0 ± 27

With these values we now want to estimate the Doppler and Power-broadening. In Fig. 20 we show the plot of the natural linewidths $\Delta\nu$ of the transitions depending on their power P . Here, only the measurements between 15 and 25 dB are shown, because the fitted results show that from 0 to 10 dB and at 30 dB the loss of atoms is saturated leading to meaningless values.

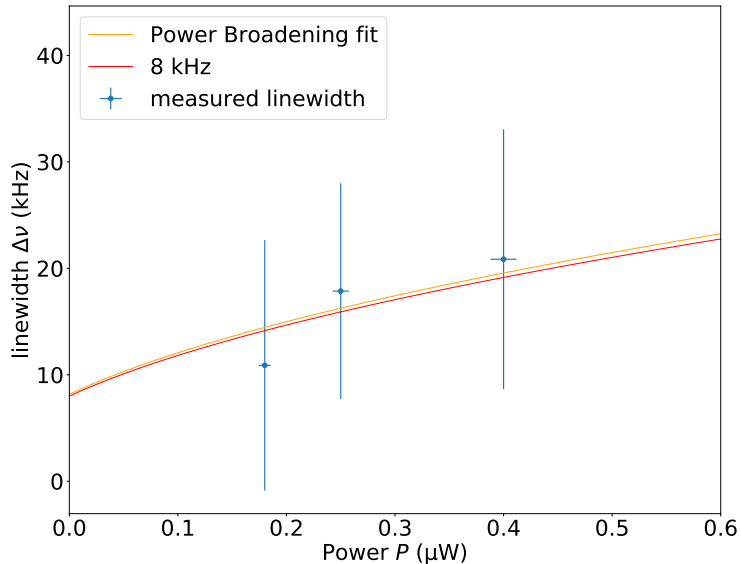


Figure 20: Power broadening in respect to the measured linewidths $\Delta\nu$ from Tab. 7 depending on the corresponding power P measured with a power meter. Here only the measured linewidths with an attenuation between 15 and 25 dB are plotted, because these measurements do not saturate the atom loss. The data points are fitted with the Power broadening Eq. (37) leading to a expected natural linewidth of $\Delta\nu = 8.2(8)$ kHz.

To estimate the Doppler broadening $\Delta\nu_D$ we first have to determine the temperature of the cloud during the observation of the transition. The temperature can be determined by considering how the width of the cloud expands during a time-of-flight (TOF) measurement. We are working with a cloud with a temperature of $T = 9.0(4) \mu\text{K}$ and inserting all the information we have such as the erbium mass m and the wavelength $\lambda = 841.22 \text{ nm}$ in Eq. (36) we get an expected Doppler broadening of $\Delta\nu_D = 59.4 \pm 1.3 \text{ kHz}$, which according to the plot in Fig. 20 does not affect our measurements. Furthermore, the estimated power broadening of the narrowest transition at 25 dB with a natural linewidth of $\Delta\nu = 8 \text{ kHz}$ is according to Eq. (37) $\Delta\nu_P = 11.5(1) \text{ kHz}$. However, plot the natural linewidths of Tab. 7, that are not saturated with their corresponding power P and fitting them with Eq.(37) leads to an expected natural linewidth of $\Delta\nu = 8.2(8) \text{ kHz}$.

5.2 Landé g-factor measurement

Applying an external magnetic field B to an atomic cloud leads to splitting an energy level with a quantum number of total angular momentum J into $2J + 1$ Zeeman levels with magnetic number m_j . This Zeeman energy shift Δf is linear and can be calculated by the following equation:

$$\Delta f = \Delta m_j \cdot B \cdot \mu_B \cdot g_J, \quad (40)$$

where Δm_j is the difference of the magnetic total angular momentum quantum number, $\mu_B = 1.4 \text{ MHz/G}$ the Bohr magneton and g the g-factor, also known as the gyromagnetic ratio.

In order to calculate the g-factor, two cases have to be considered. The first case describes the LS coupling and can be calculated by

$$g_J = 1 + (g_S - 1) \cdot \frac{J(J+1) - L(L+1) + S(S+1)}{2J(J+1)}, \quad (41)$$

where $g_S \approx 2.00232$ is the gyromagnetic ratio of the electron spin. For the ground state $^3\text{H}_6$ of erbium, $J = 6, L = 5$ and $S = 1$ lead to the value $g_J(J = 6, L = 5) = 1.167053$. Another example is the 841 nm transition of Er, where the excited state $^4\text{I}_{15/2}$ with $J = 15/2, L = 6$ and $S = 3/2$ leads to the value $g_J(J = 15/2, L = 6) = 1.200464$. The second case describes the jj coupling for excited states, where a total electronic angular momentum quantum number $J_1 = L_1 + S_1$ and $J_2 = L_2 + S_2$ must be considered. The g-factor can then be calculated by

$$g_J = g_{J_1} \cdot \frac{J(J+1) + J_1(J_1+1) - J_2(J_2+1)}{2J(J+1)} + g_{J_2} \cdot \frac{J(J+1) + J_2(J_2+1) - J_1(J_1+1)}{2J(J+1)}, \quad (42)$$

where g_{J_1} indicates the g-factor from one state and g_{J_2} the g-factor from the second state.

For the excited state of erbium corresponding to the transition in 841 nm the g-factor corresponds to $g = 1.153$ Ref.[34]. To experimentally determine the g factor, we recorded the frequency splitting between the σ^+ and the σ^- transitions depending on the magnetic field. In this case, we had a single beam of the 841 nm laser shining on the atoms in the chamber and, by changing the direction of the circular polarisation (either right- or left-handed) along the vertical B-field in the chamber, we could observe the σ^+ and the σ^- transition again as dips in the atom number. We did this process for six different magnetic fields and fitted each dip with a Lorentzian

equation (Eq. (33)) to extract the central position of the transitions. The plot on the left in Fig. 21 shows the recorded σ transitions for the B-fields 1.5 G and 3 G and the fits. With the central position of the peaks we can calculate the frequency splitting.

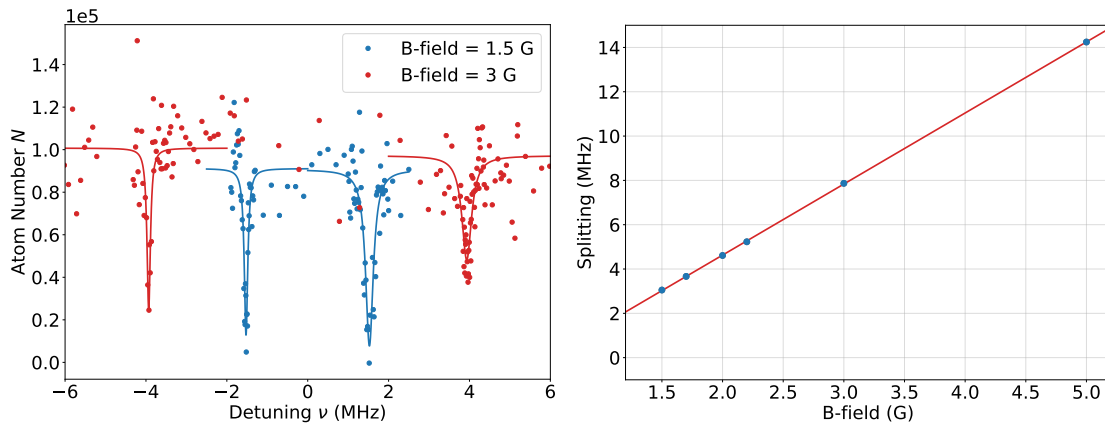


Figure 21: The left plot shows the atom number N depending on the detuning ν and two examples of the recorded σ -transitions for the B-field values of 1.5 G and 3 G. In addition, the Lorentzian fit is shown, from which the central positions of the peaks can be extracted to calculate the frequency splitting. The right plot shows the frequency splitting corresponding to each B-field value. The data points are fitted with Eq. (40) leading to the g-factor $g = 1.145(4)$.

Further, we plot the splitting depending on the B-field and determine the g-factor by fitting the data points with Eq.(40), however, with an additional offset of the magnetic field. In addition, we know that the difference of the magnetic total angular momentum quantum number is $\Delta m_j = 2$, since we are working with the σ^+ and the σ^- transitions. In the right plot in Fig. 21 the splitting corresponding to each value of the B-field is shown. The data points lead to a g-factor $g = 1.145(4)$ with a deviation of 2σ compared to the expected value. Furthermore, we obtain an offset of the B-field of $B_0 = 0.557(8)$ G, which can be caused by the calibration of the field.

6 Cooling characterisation

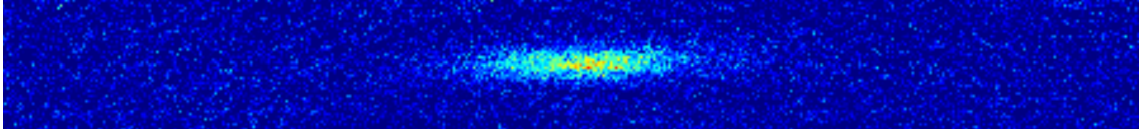
The aim of this project is to accelerate and improve the cooling and achieve faster production of the BEC by implementing narrow-line cooling. This chapter focusses on the analysis of the cooling characterisation, such as temperature measurements of the cloud from before and after the cooling, and TOF measurements to observe the expansion of the cloud while cooling. Furthermore, measurements to check the thermalisation of the cloud have been done and the cooling curve has been observed. For these measurements we observe the atoms in the chamber as shown in Fig. 8 and the setup is explained in Chap. 3.3.2. Measurements are made at a power of $0.4 \mu\text{W}$, while an OD4 ND filter (NE50A-B, Thorlabs) is mounted in front of the beam 841 nm . The power has been measured in front of the chamber, where the $\lambda/4$ plate is mounted (see Fig.8). In addition, with a TOF of 1 ms and a hold time of 500 ms we have for a MOT of 7 s a cloud of 7.5×10^5 atoms at a temperature of $21.1 \mu\text{K}$, while loading we have roughly 1×10^5 atoms at a highly fluctuating temperature of around $20 \mu\text{K}$ and lastly, while during the first evaporation step we have 1×10^5 atoms at a temperature of approximately $24 \mu\text{K}$.

6.1 Temperature measurements

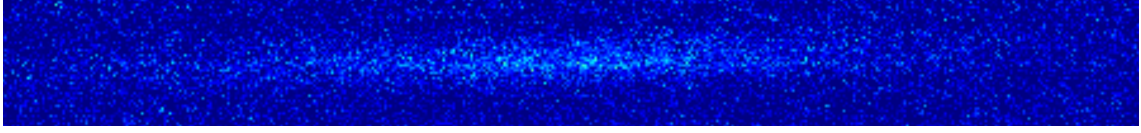
Our first measurement helps us determine the temperature of the cloud before and after applying the cooling. In this case, our sequence starts with a hold time of 500 ms after the first evaporation step, which means that we hold the atoms in the ODT. Then we apply the cooling light for 150 ms followed by 50 ms of the holding time at a 30 dB attenuation. Moreover, we did 10 ms TOF measurements to observe the expansion of the cloud. Fig. 22 shows a comparison between cold atoms, where the cloud remains more compact after the TOF, and a warm atomic cloud, which has expanded significantly more during the same TOF.

The plots in Fig. 23 show the width of the cloud σ depending on the duration of the TOF. The left plot corresponds to the x-direction, and the right plot corresponds to the y-direction of the beam. Furthermore, the red data points indicate the measurements without cooling and the blue data points are observed after cooling. The data points are fitted with the following equation [53]:

$$\sigma(t)^2 = \sigma_0^2 + \left(\sqrt{\frac{2k_{\text{B}}T}{m}} \cdot t \right)^2 \quad (43)$$



(a) cold atoms



(b) warm atoms

Figure 22: Fig. (a) shows the absorption imaging of a cold atomic cloud, while in comparison Fig. (b) shows warm atoms. A comparison between these two figures shows the expansion of the two clouds, that can be observed.

where σ_0 represents the initial cloud size, T the temperature of the cloud and t the duration of the TOF. Hence, this equation describes the size of the thermal cloud in time-of-flight measurements and allows us to extract the temperature T of the cloud while observing the change in the cloud's size.

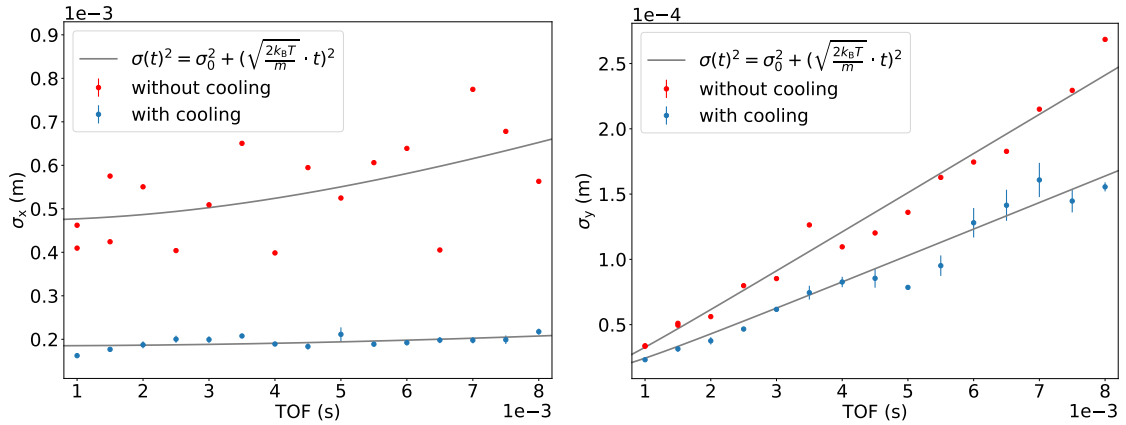


Figure 23: Atomic cloud width σ depending on the duration of the TOF. The left plot shows the x-direction of the cloud and the right the y-direction. Measurements have been done while cooling, which are represented by the blue data points. To compare the temperature before and after cooling a further measurement is done while not cooling, which are represented by the red data points. The grey lines are the fits described by Eq. (43), from which the temperature T of the cloud can be extracted.

Tab. 8 shows the results of the two plots according to the applied Eq.(43). The temperature T_x, T_y as well as the initial cloud size $\sigma_{0,x}, \sigma_{0,y}$ of each direction extracted from the fit are listed. The results show that the x-direction is cooler than the y-direction, which confirms our expectations, since this is the main direction of

the cooling beam. However, the data points recorded while not cooling for the x-direction are scattered, which complicates the initial parameters of the fit, leading to unreliable results.

Table 8: Results of the temperature T and the initial cloud size σ for both x- and y-direction extracted from Eq.(43). The results of the experiment were determined for both scenarios, with and without cooling of the atomic cloud. The corresponding fit functions, as well as the recorded data points, are shown in Fig. 23.

	T_x (μK)	T_y (μK)	$\sigma_{0,x}$ (mm)	$\sigma_{0,y}$ (μm)
with cooling	1.4(7)	4.2(2)	0.185(6)	13 ± 12
without cooling	31 ± 14	9.0(4)	0.47(4)	13 ± 17

6.2 Cooling results

Lastly, we want to observe how efficient our cooling is. We performed 2D scan measurements measuring the atom number N and the cloud size σ_x along the x-axis while varying the attenuation in steps of 5 dB between 5 and 20 dB. In this case, we had an OD5 ND filter (NE50A-B, Thorlabs) filter in front of the 841 nm laser, leading to a power of 2.410 μ W at an attenuation of 0 dB, while without the filter we would have a power of 5.295 mW at 0 dB. The power was measured for each attenuation with the aid of a powermeter (PM100D, Thorlabs) and a photodiode (S120C, Thorlabs) and is listed on Tab.9. Moreover, to observe these measurements we performed a TOF of 1 ms, followed by cooling for 100 ms and waited 50 ms before the imaging. Fig. 24 shows the atom number N of the erbium atomic cloud depending on the sideband frequency we are applying on the DDS for four different attenuations. The dip shows that at a frequency of around 570.2 MHz we reach the maximum loss of atoms. This means that the atoms get hit resonantly by the 841 nm light.

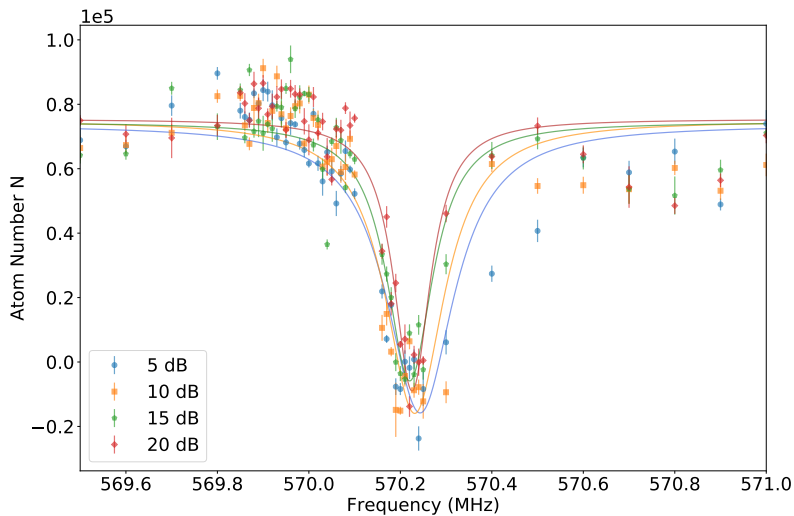


Figure 24: Atom Number N depending on frequency for four different attenuations. A few runs for better result have been done, however the measurements are for each point averaged. Additionally, the transitions are each fitted with a Lorentzian function.

Fig. 25 shows the size of the atomic cloud in the x-direction σ_x depending on the sideband frequency for four different attenuations. The central position of the dip indicates where the maximum of the cooling occurs. With the aid of these two plots we can understand in which frequency range we can cool most effectively. Therefore, the transitions are fitted with a Lorentzian function to extract the minimum of the

dips and calculate the difference. The results of the frequency ranges are listed in Tab. 9.

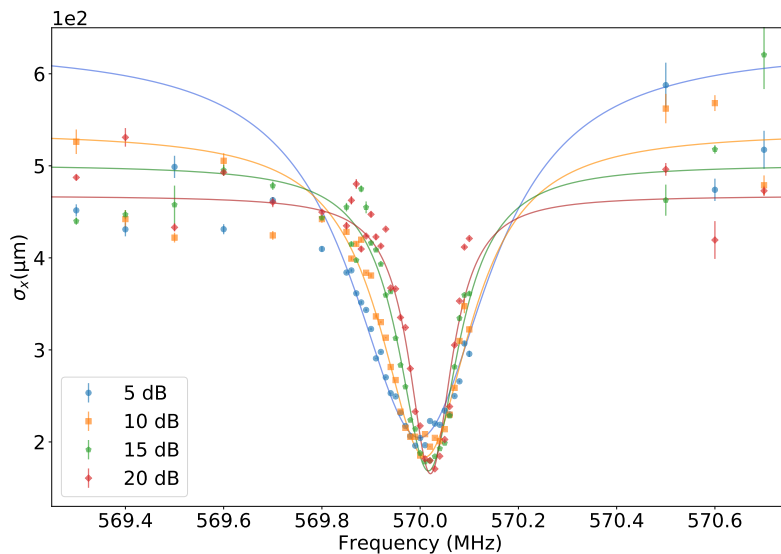


Figure 25: Cloud size of the x-direction σ_x depending on frequency for four different attenuation values. A Lorentzian fit is applied in order to extract the central position of the dip.

Fig. 26 shows the 20 dB curves from the two previous plots, plotted together and centred with respect to the resonance of the 841 nm light. The difference between the two dips corresponds to 205(4) kHz, and indicates the range where the most effective cooling occurs. This shift occurs due to the varying velocities of the atoms in the cloud and helps us to adjust the frequency such that we hit only the atoms, which are still in movement in order to cool the cloud more effectively, and lose as few atoms as possible.

Table 9: Measured power and the calculated frequency difference from Fig. 24 and 25 listed to the corresponding attenuation.

Atten. (dB)	Power (μW)	$\Delta\nu$ (MHz)
5	1.6(1)	0.244(7)
10	0.94(7)	0.221(6)
15	0.50(4)	0.204(4)
20	0.32(2)	0.205(4)

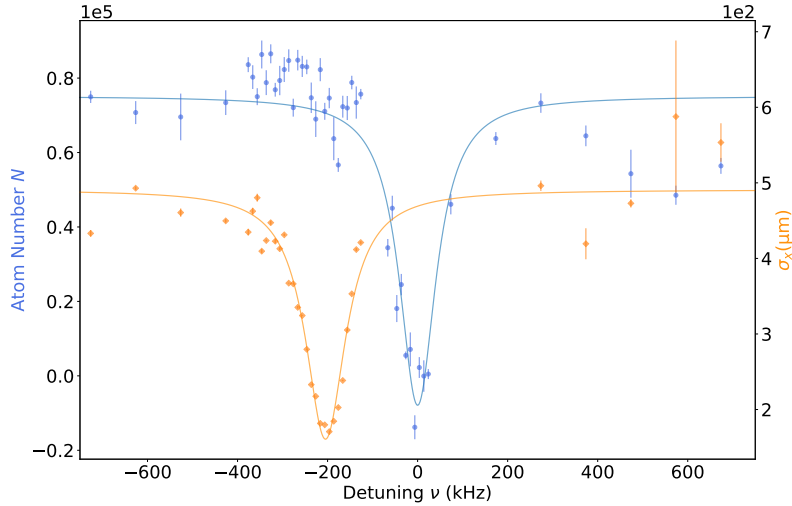


Figure 26: The right y-axis shows the atom Number N depending on the detuning ν , whereas the left y-axis represents the cloud size of the x-direction σ_x in respect to the atom number. In this case we only observe the data points for the 20 dB attenuation from Fig. 24 and 25. In addition, the range between the two dips, which corresponds to 205(4) kHz, helps us understand where the most effective cooling happens.

Finally in order to understand whether the project was effective, we want to observe the phase-space density (PSD). PSD is an important factor during the evaporation to achieve a Bose-Einstein condensation (BEC) and describes the density of atoms in both the position and momentum space. For Bose-Einstein condensation to occur in a gas of noninteracting bosonic atoms, the particles have to have a thermal de Broglie wavelength λ_{dB} larger than the mean spacing between them, which means that for the dimensionless phase-space density $\text{PSD} > 2.612$. The phase-space density of a thermal atomic cloud is determined by the temperature of the cloud and the quantum statistics of the atoms and can be expressed as:

$$\text{PSD} = n_0 \cdot \lambda_{dB}^3, \quad (44)$$

where n_0 represents the particle density and is defined as:

$$n_0 = N \cdot \bar{\omega}^3 \cdot \left(\frac{m}{2\pi k_B T} \right)^{\frac{3}{2}}. \quad (45)$$

Here N is the atom number, $\bar{\omega} = (\omega_x \omega_y \omega_z)^{\frac{1}{3}}$ the mean trap frequency, m the mass of the atoms and T their temperature. Moreover, the deBroglie wavelength is given by:

$$\lambda_{dB} = \sqrt{\frac{2\pi\hbar}{mk_B T}}. \quad (46)$$

To observe the PSD based on our measurements we calculated the temperature T by means of Eq.(43) depending on the cloud size $\sigma_x(\nu)$ from Fig.26 leading to the following equation:

$$T(\sigma_x(\nu)) = \frac{m}{2k_B t^2} \cdot (\sigma(\nu)^2 - \sigma_0^2). \quad (47)$$

In this case, we assume that the initial cloud size σ_0 is constant with the value of 0.185(6) mm taken from Tab. 8. Inserting $T(\sigma_x(\nu))$ into Eq. (44) leads to the following expression for $\rho(\nu)$ a proportional value to the PSD:

$$\rho(\nu) = N(\nu) \cdot \bar{\omega} \left(\frac{t^2}{\pi(\sigma(\nu)^2 - \sigma_0^2)} \right)^{\frac{3}{2}} \cdot \frac{2\hbar t}{m} \sqrt{\frac{\pi}{\sigma(\nu)^2 - \sigma_0^2}} \propto \text{PSD}, \quad (48)$$

with $N(\nu)$ being the recorded atom number from Fig. 26. Fig. 27 shows this equation plotted with respect to the contraction of the cloud size in the x-direction σ_x during the cooling depending on the detuning ν .

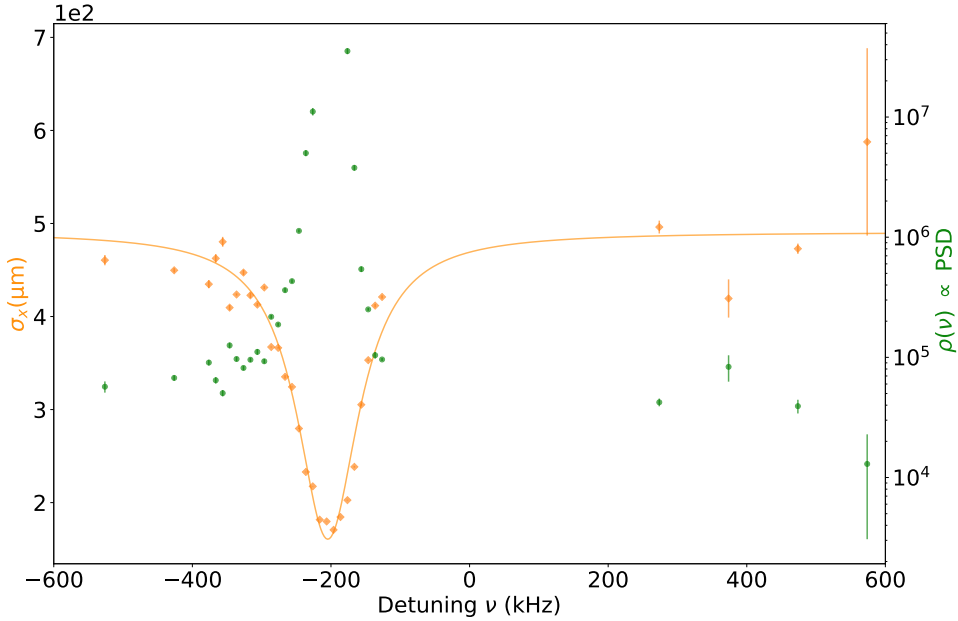


Figure 27: The left y-axis (orange data points) represents the atomic cloud size in x-direction σ_x from Fig. 25 and the right y-axis the PSD (green data points) from Eq. (48). The data points are recorded at an attenuation of 20 dB. This plot does not focus on precise values of the PSD but a proportional value in order to observe how the PSD behaves in respect to the atomic cloud size σ_x .

In this case the trap frequencies for x and y were determined from rough measurement leading to the values $\omega_x = 122 \cdot 2\pi$ Hz and $\omega_y = 7 \cdot 2\pi$ Hz. For the z-direction, we were unable to calculate the trap frequency because of the low number of atoms in the trap. Thus, the trap frequency in the z-direction is roughly estimated to be

around $\omega_z = 500 \cdot 2\pi$ Hz according to previous measurements. Furthermore, the duration of the TOF t for these data points is $t = 1$ ms. However, the aim of this graph is not an exact value of the PSD but an approximate value proportional to the PSD to observe how the PSD would change with respect to the size of the atomic cloud σ_x . Unfortunately, a precise PSD value cannot be calculated since the conditions of the experiment, such as having enough atoms in the trap, were not as good as expected. The larger the PSD value and the atom number in a dipole trap, the faster a BEC can be produced. Nevertheless, all the plots show some efficient cooling of the atomic cloud consisting of erbium, which was the goal of this project. In addition, since a similar experimental setup has been set for dysprosium atoms, the same procedure is planned to be applied onto a dysprosium atomic cloud. Although the laser is adjusted to shine on the atomic cloud, we have not tested it yet.

7 Conclusion and Outlook

This thesis focusses on a laser cooling technique of the rare-earth metal erbium and dysprosium using their narrow transitions with a linewidth in the range of kHz. Although cooling can be achieved with transitions with a broader linewidth, narrower transitions enable us to reach an even lower temperature, allowing us to cool more and faster.

In this project, we used for erbium the transition $6s^2\ ^3H_6 \rightarrow\ ^4I_{15/2}^o 5d_{5/2} 6s^2$ with a wavelength of $\lambda_{Er} = 841.22\text{ nm}$ and a linewidth of $\Gamma_{Er} = 2\pi \cdot 8.0\text{ kHz}$ and for dysprosium the transition $6s^2\ ^5I_8 \rightarrow\ ^6H^o 5d 6s^2 5K_9^o$ with $\lambda_{Dy} = 740.96\text{ nm}$ and $\Gamma_{Dy} = 2\pi \cdot 1.78\text{ kHz}$.

The laser cooling is achieved by applying the technique of the optical molasses, which in our case consists of two pairs of counterpropagating laser beams instead of three. Therefore, a laser setup has been set consisting of two laser beams, a laser with wavelengths of $\lambda = 841\text{ nm}$ laser for erbium and $\lambda = 741\text{ nm}$ for dysprosium. These two laser beams were led to an SLS cavity by using optical elements such as mirrors and lenses, as well as electronic components such as EOMs to control the phase of the light or AOMs to lead the beam to the main experiment. The cavity with a length of 100 mm and a diameter of 50 mm leading to a free spectral range of 1.49 GHz is a very important component of the optical setup and is necessary to narrow down the linewidth of our laser beams in order to be able to address the narrow transitions we are aiming for. To stabilise the lasers to the needed frequencies we went for the PDH locking technique, which was practical for this project, since we are working with two lasers and the cavity covered both wavelengths with its range of the high reflectance, while other techniques might need separate elements for each wavelength. Moreover, the cavity was characterised using both lasers that lead for 741 nm to the linewidth $\Gamma = 94.0(2)\text{ kHz}$, finesse $\mathcal{F} = 15\,853(31)$ and storage time $\tau_p = 1.708(3)\ \mu\text{s}$. For $\lambda = 841\text{ nm}$ it resulted in $\Gamma = 89.6(9)\text{ kHz}$, $\mathcal{F} = 16\,630(270)$, and $\tau_p = 1.78(3)\ \mu\text{s}$.

The analysis in this thesis is focused only on the erbium element, since the laboratory was working with that element at that time. First, the analysis focusses on a transition characterisation followed by a cooling characterisation.

In the section on transition characterisation, the search process of the transition is explained. Furthermore, we determine the linewidth while considering the broadening mechanisms that affect the linewidth. According to the theory the transition had to be found at the wavelength $\lambda = 841.219\,56\text{ nm}$, which is the region where we

scanned the piezovoltage to tune the frequency and find the a dip on our screens marking the transition. We have found two transitions, one at 841.2250 nm and another at 841.2201 nm. Although the second value is closer to the theoretical value, a superficial analysis has shown that some important parameters, such as the natural linewidth $\Delta\nu$ of the transition and the g -factor, did not match the expected values. Hence, we assume that this transition could possibly be caused by photoassociation, or another problem could be that the wavemeter is not calibrated correctly anymore. We anticipated a natural linewidth of 8 kHz, yet the narrowest linewidth we calculated was 24.8(8) kHz. It is likely that the Power and Doppler broadening had an effect on the linewidth in our experiment. In addition, we determined the g -factor by observing the splitting between the σ^+ and σ^- transitions while varying the B -field. Data points led to a g -factor of the value 1.145(4), while according to the theoretical parameters we should expect a g -factor of the value 1.153.

In the section of the cooling characterisation, we focus on some temperature measurements as well as some cooling results. We measured the temperature in the x- and y-direction of the trap while observing the cloud size and found after cooling a temperature of $T_x = 1.4(7) \mu\text{K}$ with a cloud size of $\sigma_{0,x} = 0.185(6) \text{ mm}$ for the x-direction and $T_y = 4.2(2) \mu\text{K}$ with $\sigma_{0,y} = 13 \pm 12 \mu\text{m}$ for the y-direction.

For cooling characterisation, we recorded a 2D scan of the atom number N and the cloud size σ_x in the x-direction depending on the frequency applied on DDS. Data points were recorded for four different attenuations. From these measurements, the difference between the two dips was determined, which indicated the range where the most effective cooling occurs without losing too many atoms. Additionally, for a better cooling comparison, we tried to measure the PSD. However, since we did not have sufficient atoms in the trap, the trap frequency could not be measured. Instead, a proportional to the PSD value $\rho(\nu)$ has been analysed. The value $\rho(\nu)$ was calculated using 2D scans and assuming that the initial cloud size remains constant. Nevertheless, all of the results of the analysis led to some efficient cooling using the narrow transitions of the erbium element.

A further outlook of this project is to try the whole process for dysprosium and to analyse the transition as well as the cooling. In addition, since the main experiment focusses on mixtures of both elements, a further task in the future would be to try the cooling also for mixtures of Er and Dy.

Appendix A

In this appendix belongs to the chapter of the linewidth measurement and broadening mechanisms. We performed atom loss spectroscopy and plotted the dips as plots of the atom number N depending on the detuning ν . This measurement has been made for seven different attenuations, namely, from 0 to 30 dB. The dips were then fitted with a Lorentzian, a Gaussian, and a Voigt fit, from which the chi-square χ^2 parameter is determined and compared to find the most suitable fits. Tab. 10 shows that the Voigt function leads to the most suitable fits.

Table 10: Comparison of a Lorentzian, a Gaussian and a Voigt fit applied onto atom loss spectroscopy at seven different attenuations. The chi-square χ^2 value is determined and compared showing that the Voigt function leads to the most meaningful fits.

Atten. (dB)	Gauss			Lorentz			Voigt			
	$\Delta\nu$ (kHz)	χ^2	red. χ	$\Delta\nu$ (kHz)	χ^2	red. χ	$\Delta\nu_G$ (kHz)	$\Delta\nu_L$ (kHz)	χ^2	red. χ
0	102(5)	2.63×10^{10}	3.19×10^8	117(10)	3.42×10^{10}	4.17×10^8	108(23)	20 ± 40	2.67×10^{10}	3.30×10^8
5	88(4)	9.78×10^9	2.28×10^8	104(9)	1.45×10^{10}	3.37×10^8	78 ± 23	30 ± 40	9.50×10^9	2.26×10^8
10	69.6 ± 2.6	2.14×10^{10}	2.44×10^8	82(5)	2.82×10^{10}	3.21×10^8	82 ± 12	0 ± 22	2.14×10^{10}	2.47×10^8
15	52.5 ± 2.0	3.88×10^{10}	3.23×10^8	54.8 ± 3.2	4.17×10^{10}	3.48×10^8	47(9)	21 ± 12	3.82×10^{10}	3.21×10^8
20	34.6 ± 1.8	3.18×10^{10}	3.83×10^8	36.5 ± 2.8	3.24×10^{10}	3.90×10^8	29(8)	18 ± 10	3.07×10^{10}	3.75×10^8
25	34.5 ± 1.9	2.34×10^{10}	2.16×10^8	37.7 ± 3.2	2.53×10^{10}	2.34×10^8	34(8)	11 ± 12	2.31×10^{10}	2.16×10^8
30	30(6)	1.69×10^{10}	2.56×10^8	27(8)	1.87×10^{10}	2.84×10^8	35 ± 19	0 ± 32	1.69×10^{10}	2.60×10^8

References

- [1] E. S. Shuman, J. F. Barry, and D. DeMille. Laser cooling of a diatomic molecule. *Nature*, 467(7317):820–823, sep 2010.
- [2] Matthew T. Hummon, Mark Yeo, Benjamin K. Stuhl, Alejandra L. Collopy, Yong Xia, and Jun Ye. 2d magneto-optical trapping of diatomic molecules. *Physical Review Letters*, 110(14), apr 2013.
- [3] J. F. Barry, D. J. McCarron, E. B. Norrgard, M. H. Steinecker, and D. DeMille. Magneto-optical trapping of a diatomic molecule. *Nature*, 512(7514):286–289, aug 2014.
- [4] Peter Horak, Jean-Yves Courtois, and Gilbert Grynberg. Atom cooling and trapping by disorder. *Physical Review A*, 58(5):3953–3962, nov 1998.
- [5] F. Schmidt-Kaler, J. Eschner, G. Morigi, C.F. Roos, D. Leibfried, A. Mundt, and R. Blatt. Laser cooling with electromagnetically induced transparency: application to trapped samples of ions or neutral atoms. *Applied Physics B*, 73(8):807–814, dec 2001.
- [6] E. A. Curtis, C. W. Oates, and L. Hollberg. Quenched narrow-line laser cooling of $^{40}\text{Ca}^+$ near the photon recoil limit. *Physical Review A*, 64(3), Aug 2001.
- [7] Mingwu Lu, Seo Ho Youn, and Benjamin L. Lev. Spectroscopy of a narrow-line laser-cooling transition in atomic dysprosium. *Phys. Rev. A*, 83:012510, Jan 2011.
- [8] P. M. Duarte, R. A. Hart, J. M. Hitchcock, T. A. Corcovilos, T.-L. Yang, A. Reed, and R. G. Hulet. All-optical production of a lithium quantum gas using narrow-line laser cooling. *Physical Review A*, 84(6), dec 2011.
- [9] Daniil Provorchenko, Dmitry Tregubov, Denis Mishin, Mikhail Yaushev, Denis Kryuchkov, Vadim Sorokin, Ksenia Khabarova, Artem Golovizin, and Nikolay Kolachevsky. Deep laser cooling of thulium atoms to sub- μK temperatures in magneto-optical trap. *Atoms*, 11(2):30, feb 2023.
- [10] Y. N. Martinez de Escobar, P. G. Mickelson, M. Yan, B. J. DeSalvo, S. B. Nagel, and T. C. Killian. Bose-einstein condensation of ^{84}Sr . 2009.

- [11] Jens Ulitzsch, Daniel Babik, Roberto Roell, and Martin Weitz. Bose-einstein condensation of erbium atoms in a quasiolelectrostatic optical dipole trap. *Physical Review A*, 95(4), apr 2017.
- [12] Albert Frisch, Kiyotaka Aikawa, Michael Mark, Francesca Ferlaino, Ekaterina Berseneva, and Svetlana Kotochigova. Hyperfine structure of laser-cooling transitions in fermionic erbium-167. *Physical Review A*, 88(3), sep 2013.
- [13] Ch. Gross, H. C. J. Gan, and K. Dieckmann. All-optical production and transport of a large 6li quantum gas in a crossed optical dipole trap. *Physical Review A*, 93(5), may 2016.
- [14] Simon Stellmer, Florian Schreck, and Thomas C. Killian. DEGENERATE QUANTUM GASES OF STRONTIUM. In *Annual Review of Cold Atoms and Molecules*, pages 1–80. WORLD SCIENTIFIC, mar 2014.
- [15] Thomas H. Loftus, Tetsuya Ido, Andrew D. Ludlow, Martin M. Boyd, and Jun Ye. Narrow line cooling: Finite photon recoil dynamics. *Phys. Rev. Lett.*, 93:073003, Aug 2004.
- [16] Sebastian Kraft, Felix Vogt, Oliver Appel, Fritz Riehle, and Uwe Sterr. Bose-einstein condensation of alkaline earth atoms:40ca. *Physical Review Letters*, 103(13), sep 2009.
- [17] Rahul Sawant and S. A. Rangwala. Lasing by driven atoms-cavity system in collective strong coupling regime. *Scientific Reports*, 7(1), sep 2017.
- [18] Xiaobin Ma, Zhuxiong Ye, Liyang Xie, Zhen Guo, Li You, and Meng Khoon Tey. A dual-species magneto-optical trap for lithium and strontium atoms. 2019.
- [19] E. Anne Curtis, Christopher W. Oates, and Leo Hollberg. Quenched narrow-line second- and third-stage laser cooling of ^{40}Ca . *Journal of the Optical Society of America B*, 20(5):977, may 2003.
- [20] S. Snigirev, A. J. Park, A. Heinz, I. Bloch, and S. Blatt. Fast and dense magneto-optical traps for strontium. *Physical Review A*, 99(6), jun 2019.
- [21] Andrew J. Berglund, James L. Hanssen, and Jabez J. McClelland. Narrow-line magneto-optical cooling and trapping of strongly magnetic atoms. *Physical Review Letters*, 100(11), mar 2008.

- [22] A. Frisch, K. Aikawa, M. Mark, A. Rietzler, J. Schindler, E. Zupanič, R. Grimm, and F. Ferlaino. Narrow-line magneto-optical trap for erbium. *Phys. Rev. A*, 85:051401, May 2012.
- [23] Ryuta Yamamoto, Jun Kobayashi, Takuma Kuno, Kohei Kato, and Yoshiro Takahashi. An ytterbium quantum gas microscope with narrow-line laser cooling. *New Journal of Physics*, 18(2):023016, feb 2016.
- [24] N Malossi, S Damkjær, PL Hansen, LB Jacobsen, L Kindt, Sebastien Sauge, JW Thomsen, FC Cruz, Maria Allegrini, and Ennio Arimondo. Two-photon cooling of magnesium atoms. *Physical Review A*, 72(5):051403, 2005.
- [25] T Binnewies, G Wilpers, U Sterr, F Riehle, J Helmcke, TE Mehlstäubler, Ernst Maria Rasel, and Wolfgang Ertmer. Doppler cooling and trapping on forbidden transitions. *Physical Review Letters*, 87(12):123002, 2001.
- [26] Thomas H. Loftus, Tetsuya Ido, Martin M. Boyd, Andrew D. Ludlow, and Jun Ye. *Narrow line cooling and momentum-space crystals*, volume 70. American Physical Society, Dec 2004.
- [27] Takashi Mukaiyama, Hidetoshi Katori, Tetsuya Ido, Ying Li, and Makoto Kuwata-Gonokami. Recoil-limited laser cooling of sr 87 atoms near the fermi temperature. *Physical review letters*, 90(11):113002, 2003.
- [28] Royal Society of Chemistry. Erbium. [https://www.rsc.org/...](https://www.rsc.org/) [Online; last access 22.12.2021].
- [29] P. Enhang. *Encyclopedia of the Elements: Technical Data - History - Processing - Applications*. Wiley, 2008.
- [30] Royal Society of Chemistry. Dysprosium. [https://www.rsc.org/...](https://www.rsc.org/) [Online; last access 22.12.2021].
- [31] J.-C.G. Bunzli and V.K. Pecharsky. *Handbook on the Physics and Chemistry of Rare Earths, Volume 59, Including Actinides*. Elsevier Science & Technology, 2021.
- [32] T Lahaye, C Menotti, L Santos, M Lewenstein, and T Pfau. The physics of dipolar bosonic quantum gases. *Reports on Progress in Physics*, 72(12):126401, Nov 2009.

- [33] A. Patscheider, B. Yang, G. Natale, D. Petter, L. Chomaz, M. J. Mark, G. Hovhannesian, M. Lepers, and F. Ferlaino. Observation of a narrow inner-shell orbital transition in atomic erbium at 1299 nm. *Physical Review Research*, 3(3), Sep 2021.
- [34] W. C. Martin, R. Zalubas, and L. Hagan. *Atomic energy levels - the rare earth elements. (the spectra of lanthanum, cerium, praseodymium, neodymium, promethium, samarium, europium, gadolinium, terbium, dysprosium, holmium, erbium, thulium, ytterbium, and lutetium). [66 atoms and ions]*. United States, 1978. Research Org.: Manchester Coll. of Science and Technology (UK). Dept. of Chemistry.
- [35] Daniel A. Steck. *Cesium D Line Data*, volume revision 2.2.1. 21 Nov 2019.
- [36] C.J. Foot. *Atomic physics*. Oxford master series in physics. Oxford University Press, 2005.
- [37] H Ban, M Jacka, James Hanssen, Joseph Reader, and Jabez McClelland. Laser cooling transitions in atomic erbium. (13), 2005-04-18 00:04:00 2005.
- [38] T.W. Hänsch and A.L. Schawlow. Cooling of gases by laser radiation. *Optics Communications*, 13(1):68–69, 1975.
- [39] P. D. Lett, W. D. Phillips, S. L. Rolston, C. E. Tanner, R. N. Watts, and C. I. Westbrook. *Optical molasses*, volume 6. 1989.
- [40] Maximilian Sohmen. *Supersolidity in Dipolar Quantum Gases in and out of Equilibrium*. Universität Innsbruck, 2021.
- [41] P. Ilzhöfer, G. Durastante, A. Patscheider, A. Trautmann, M. J. Mark, and F. Ferlaino. Two-species five-beam magneto-optical trap for erbium and dysprosium. *Phys. Rev. A*, 97:023633, Feb 2018.
- [42] Albert Frisch. *Dipolar quantum gases of erbium*. Universität Innsbruck, 2014.
- [43] Philipp Ilzhöfer. *Creation of Dipolar Quantum Mixtures of Erbium and Dysprosium*. Universität Innsbruck, 2020.
- [44] Matthew A Norcia, Claudia Politi, Lauritz Klaus, Elena Poli, Maximilian Sohmen, Manfred J Mark, Russell N Bisset, Luis Santos, and Francesca Ferlaino. Two-dimensional supersolidity in a dipolar quantum gas. *Nature*, 596(7872):357–361, 2021.

- [45] Gianmaria Durastante. *Creation of Erbium-Dysprosium Dipolar Quantum Mixtures and Their Interspecies Feshbach Resonances*. Universität Innsbruck, 2020.
- [46] Simon Baier. *An optical dipole trap for Erbium with tunable geometry*. Universität Innsbruck, 2012.
- [47] Claudia Politi. *Optical dipole trap for an erbium and dysprosium mixture*. Universität Innsbruck, 2017.
- [48] Jürgen Eichler and Hans-Joachim Eichler. *Laser: Bauformen, Strahlführung, Anwendungen*. Springer Berlin / Heidelberg, 2010.
- [49] Bahaa EA Saleh and Malvin Carl Teich. *Fundamentals of photonics*. John Wiley & sons, 2019.
- [50] Wolfgang Demtröder. *Experimentalphysik 3: Atome, Moleküle und Festkörper*. Springer-Verlag, 2010.
- [51] Eric D. Black. An introduction to pound–drever–hall laser frequency stabilization. *American Journal of Physics*, 69:79–87, 1 2001.
- [52] M. Nickerson. A review of pound-drever-hall laser frequency locking. *JILA, University of Colorado and NIST*, 2019.
- [53] Wolfgang Ketterle, Dallin S Durfee, and DM Stamper-Kurn. Making, probing and understanding bose-einstein condensates. *arXiv preprint cond-mat/9904034*, 1999.

Acknowledgements

First, I would like to thank my supervisor Francesca Ferlaino for giving me the opportunity to be part of the Er-Dy lab and in general of her group in Innsbruck and for giving me such an interesting project for my master thesis. I appreciate her support and feedback. I am grateful to Manfred Mark for all the help and for taking the time to review and correct my thesis. I am also thankful for the encouragement he provided to help me complete this project. A huge thank you goes to all the members of the group, consisting of the Er-Dy, Erbium and T-Reqs lab as well as the theory group. Thank you helping me when I had questions or even borrowing electronic components, for nice lunch breaks and for the fun activities. I am especially grateful to the members of the Er-Dy lab. I thank Matthew Norcia for helping me with my optical setup, as well as for teaching me many important things in the lab and being there to answer my questions. I also thank Lauritz Klaus for voluntarily wanting me to keep him updated and for his help and corrections throughout the thesis process. I thank Claudia Politi for the corrections and the discussions, Eva Casotti for the support while performing the measurements but also while realigning the lasers, Maximilian Sohmen for the conversations, and Clemens Ulm for wanting 'to get rid of me' from the lab. A big thanks goes to the administrative support at the University of Innsbruck and the Institute for Quantum Optics and Quantum Information (IQOQI), to Silvia Bonazza, Elisabeth Huck, Nikolaus Falschunger and David Jordan and, of course, to Gerhard Hendl from the electronic workshop, who prepared my electronic components and repaired everything I broke.

I am very grateful to my friend Simon Gschwendtner for always being there to help me and answer my questions regardless of whether they were about physics or about programming. This thesis would have been much more difficult without your help. Further, I would like to thank all my university friends for the great breaks, but special thanks go to Amal El Arrach, with whom I shared my office, and we had a great time, Ariane Kronthaler for joining me in the library and thus making the writing sessions more fun, but also my friends outside the physics world, who made my life in Innsbruck during my studies an unforgettable chapter of my life.

Lastly, but most importantly, I would like to thank my family for making it possible for me to study physics in such a beautiful city but also thank you for the encouragement and for always being there for me during this whole journey.



Eidesstattliche Erklärung

Ich erkläre hiermit an Eides statt durch meine eigenhändige Unterschrift, dass ich die vorliegende Arbeit selbständig verfasst und keine anderen als die angegebenen Quellen und Hilfsmittel verwendet habe. Alle Stellen, die wörtlich oder inhaltlich den angegebenen Quellen entnommen wurden, sind als solche kenntlich gemacht.

Die vorliegende Arbeit wurde bisher in gleicher oder ähnlicher Form noch nicht als Magister-/Master-/Diplomarbeit/Dissertation eingereicht.

Datum

Unterschrift